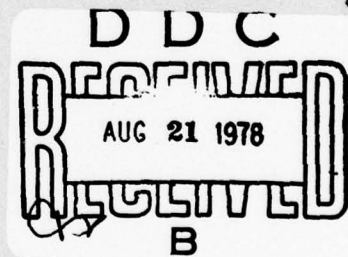(12)

SU

6/30

ade000179

Shallow Water Acoustics

Summary Report (First Phase)

F. INGENITO, R. H. FERRIS, W.A. KUPERMAN, AND S.N. WOLF

Applied Ocean Acoustics Branch
Acoustics Division

LEVEL II

March 27, 1978

NAVAL RESEARCH LABORATORY
Washington, D.C.

78 06 29 010

REPORT DOCUMENTATION PAGE		READ INSTRUCTIONS BEFORE COMPLETING FORM
1. REPORT NUMBER NRL Report 8179	2. GOVT ACCESSION NO.	3. RECIPIENT'S CATALOG NUMBER
4. TITLE (and Subtitle) SHALLOW-WATER ACOUSTICS, SUMMARY REPORT (FIRST PHASE)		5. TYPE OF REPORT & PERIOD COVERED Interim report on a continuing NRL problem
		6. PERFORMING ORG. REPORT NUMBER
7. AUTHOR(s) F. Ingenito, R. H. Ferris, W. A. Kuperman, and S. N. Wolf		8. CONTRACT OR GRANT NUMBER(s)
9. PERFORMING ORGANIZATION NAME AND ADDRESS Naval Research Laboratory Washington, DC 20375		10. PROGRAM ELEMENT, PROJECT, TASK AREA & WORK UNIT NUMBERS NRL Problem S01-94B Element 62759N Project SF52552691
11. CONTROLLING OFFICE NAME AND ADDRESS Naval Sea Systems Command, Washington, DC 20362 and Office of Naval Research, Arlington, VA 22217		12. REPORT DATE March 27, 1978
		13. NUMBER OF PAGES 56
14. MONITORING AGENCY NAME & ADDRESS(if different from Controlling Office)		15. SECURITY CLASS. (of this report) UNCLASSIFIED
		15a. DECLASSIFICATION/DOWNGRADING SCHEDULE
16. DISTRIBUTION STATEMENT (of this Report) Approved for public release; distribution unlimited		
17. DISTRIBUTION STATEMENT (of the abstract entered in Block 20, if different from Report)		
18. SUPPLEMENTARY NOTES		

19. KEY WORDS (Continue on reverse side if necessary and identify by block number)

Absorption	Range-dependent environment
Arbitrary sound-speed profile	Shallow water acoustics
Bottom and surface roughness	Solid subbottom
Fluid subbottom	Spatial filter
Normal-mode theory	Transmission loss

20. ABSTRACT (Continue on reverse side if necessary and identify by block number)

In response to the Navy's need for a submarine warfare capability in shallow-water areas of the oceans, NRL has been conducting a research program in shallow-water acoustics. The goal of the first phase of this program has been to determine if wave theory can be used to predict the acoustic field at long ranges from a submerged acoustic source. The approach used an iterative process involving trial models and at-sea measurements. The wave equation for the physical model is solved by numerical methods and implemented on a high-speed general-purpose computer. Since the

(Continued)

DD FORM 1473 EDITION OF 1 NOV 65 IS OBSOLETE
1 JAN 73
S/N 0102-LF-014-6601

i

20. Abstract (Continued)

acoustic field at long ranges is propagated in the discrete normal modes of the duct, special experimental methods were used to resolve individual modal fields so that their measured characteristics could be compared with predictions. This report presents a detailed description of the NRL normal-mode model in its current form and describes the experimental evaluation procedures and results. Salient features of the model include variable sound speed in the water, slowly variable water depth, statistically rough boundaries, sediment layering, and both shear-wave and compressional-wave propagation in the bottom. Although certain recognized problems remain to be solved, it has been demonstrated that the model can in most cases predict the characteristics of the signal field with sufficient accuracy to be a useful tool in system design, performance prediction, and tactics.

CONTENTS

iii

SHALLOW WATER ACOUSTICS

SUMMARY REPORT (FIRST PHASE)

INTRODUCTION

In ocean areas of shallow or intermediate water depth acoustic propagation is almost always influenced profoundly by the proximity of the sea bottom. This is in contrast to the deep ocean basins, where the omnipresent positive sound-speed gradient at great depths reduces acoustic interactions with the bottom to a minor role in many applications. Understanding and predicting acoustic performance in shallow water is further complicated by the relatively high temporal and spatial variability of environmental parameters usually encountered in these areas. In general, detection range in shallow water is severely limited both by the high attenuation which results from interaction with the bottom and by the limited water depth, which will not support the long-range propagation paths (convergence zone and bottom bounce) available in deep water.

Wave-theory analysis [1] has shown that at all except very short ranges propagation occurs in discrete normal-modes of the shallow-water duct. A normal-mode model useful for predicting propagation phenomena must accommodate the following environmental parameters:

- Variable water depth,

- Statistically rough boundaries,

- Sediment layering,

- Both shear-wave and compressional-wave propagation in the bottom, and

- Variable sound speed in the water both in depth and in range.

A research program within the Acoustics Division at NRL has been addressing the shallow-water problem. The first phase of this work, dealing with the signal field, has been completed, and the results are the subject of this report. The program goal has been to develop tested models of acoustic propagation useful for sonar performance prediction and selection of optimum operating procedures and to guide the Navy in designing sonars to improve their effectiveness in shallow water. The approach has been to start with the simple Pekeris [2] normal-mode model and to extend it as necessary, making full use of current computer technology. Each stage of development is tested experimentally at sea.

The program to date has been concerned principally with the basic question of whether a mathematical model can predict the modal characteristics of shallow-water propagation in an

1

ocean environment. The characteristics of interest are: the degree to which each of the normal modes is excited by a point source in the duct, the vertical pressure amplitude distribution in each modal field, the group and phase velocity of each modal field, the attenuation of individual modal fields due to a lossy bottom, and the effects of statistical perturbations of the boundaries. Models for predicting the first four of these characteristics have been evaluated through experiments conducted in each of three geographical areas having markedly differing environmental characteristics. Special experimental techniques were devised to permit measurements on individual modal fields. The fifth characteristic, concerning the effect of scattering, has been approached through the development of a wave-theory scattering model for shallow-water ducts having statistically rough boundaries. The scattering theory has not yet been experimentally confirmed.

Recent efforts have addressed the problem of predicting transmission loss in shallow water. In a normal-mode formulation the signal field is the sum of all the appropriate normal-mode terms with attenuation included. Prediction of transmission loss involves the calculation of the excitation, geometric spreading, and attenuation of each modal field and the summation of modal components at designated field points. The NRL transmission-loss model uses the outputs of the normal-mode model with one further modification. On long propagation paths it is necessary to account for the effect of horizontal variations in the physical properties of the duct, including changing water depth. At present an adiabatic approximation is used in which the mode functions and attenuation coefficients are computed using local conditions as inputs, so that they are assumed to be slowly varying functions of range. Prefatory tests of the model have been conducted against data from selected shallow-water areas including data taken over gently sloping bottoms.

At the present stage of development the NRL model can take into account the following environmental configurations:

- A sound-speed profile which is an arbitrary function of depth,
- The major attenuation mechanisms (absorption in the bottom and scattering at the boundaries),
- A bottom which can be composed of layers of different densities and sound speeds, of which the semi-infinite layer can support shear, and
- A slowly varying water depth and sound-speed profile as a function of range.

THEORY

Signal Field

The ocean bottom in 'shallow-water areas is characterized by several layers of unconsolidated sediment overlying deeper, high-velocity rock layers. Usually the unconsolidated layers are thick enough that the deeper layers have negligible effect on an acoustic signal propagated in the water. The high-speed layers can therefore be neglected, and the unconsolidated layers can be considered to extend to infinity. Unconsolidated sediments can be assumed to behave like fluids, but the rock layers must be treated as isotropic solids capable of supporting shear. Occasionally the rock layers are close to the surface and their effect becomes important.

With these facts in mind we have developed two idealized models of the shallow-water environment which we feel are adequate to treat most cases. The first is a three-layer fluid model consisting of a layer of constant-density water having a sound speed dependent only on

2

depth and overlying a bottom consisting of two fluid layers. The upper bottom layer also has constant density and a sound speed dependent on depth, and the second bottom layer is a semi-infinite constant-density fluid having a sound speed that is constant. The second model is the same as the first except that the final semi-infinite layer is an isotropic solid having constant compressional-wave speed, shear-wave speed, and density.

These two models are formulated for range-independent, nonlossy media with smooth parallel boundaries. Attenuation due to bottom loss and attenuation due to surface and bottom scattering are later added as perturbations. Both models and their refinements will now be discussed in detail.

Three-Fluid Model in the Ideal Case of No Attenuation

The geometry of the ideal three-fluid model is shown in Fig. 1. A fluid layer of thickness H_1, constant density ρ_1, and depth-dependent sound speed $c_1(z)$ is bounded above by a pressure-release surface and below by a second fluid layer of constant density ρ_2, depth-dependent sound speed $c_2(z)$, and thickness H_2. The third layer is a semi-infinite fluid with constant density ρ_3 and sound speed c_3. A Cartesian coordinate system is defined so that the pressure-release surface lies in the xy plane and the z axis is perpendicular to the surface with z increasing downward.

Fig. 1 — The geometry of the ideal three-fluid model
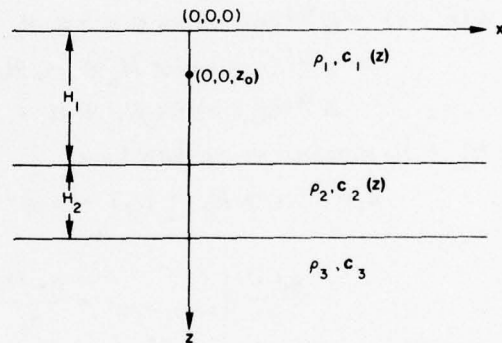
A harmonic point source of unit source strength is on the z axis at depth z_0, and it is desired to calculate the sound field at the point (x, y, z). At any point in the medium the velocity potential $\phi(x, y, z)$ satisfies the equation

$$\nabla^2\phi + \left[\frac{\omega}{c(z)}\right]^2 \phi = -\delta(x)\,\delta(y)\,\delta(z - z_0), \tag{1}$$

where we have dropped the time dependence $e^{-i\omega t}$, in which ω is the angular frequency of the source, and where

$$c(z) = c_1(z) \text{ for } 0 \leqslant z \leqslant H_1,$$
$$= c_2(z) \text{ for } H_1 \leqslant z \leqslant H_1 + H_2,$$
$$= c_3 \text{ for } H_1 + H_2 \leqslant z < \infty.$$

3

It should be noted that if the source is not harmonic but emits a pulse $f(t)$, the velocity potential $\Phi(x, y, z, t)$ is

$$\Phi(x, y, z, t) = \frac{1}{2\pi} \int_{-\infty}^{\infty} g(\omega)\phi(x, y, z, \omega)e^{-i\omega t} d\omega, \tag{2}$$

where

$$g(\omega) = \int_{-\infty}^{\infty} f(t)e^{i\omega t} dt$$

and $\phi(x, y, z, \omega)$ is the solution of Eq. (1).

At each of the interfaces we have boundary conditions. At the surface the pressure-release condition means that

$$\phi(x, y, 0) = 0. \tag{3}$$

At the interface $z = H_1$ the continuity of pressure gives

$$\rho_1 \phi^{(1)}(x, y, H_1) = \rho_2 \phi^{(2)}(x, y, H_1) \tag{4}$$

and the continuity of the normal component of particle velocity gives

$$\left. \frac{\partial \phi^{(1)}}{\partial z} \right|_{z=H_1} = \left. \frac{\partial \phi^{(2)}}{\partial z} \right|_{z=H_1}. \tag{5}$$

We have introduced the notation

$$\phi(x, y, z) = \phi^{(1)}(x, y, z) \text{ for } 0 \leqslant z \leqslant H_1,$$
$$= \phi^{(2)}(x, y, x) \text{ for } H_1 \leqslant z \leqslant H_1 + H_2,$$
$$= \phi^{(3)}(x, y, z) \text{ for } H_1 + H_2 \leqslant z < \infty.$$

At the $z = H_1 + H_2$ interface we similarly have

$$\rho_2 \phi^{(2)}(x, y, H_1 + H_2) = \rho_3 \phi^{(3)}(x, y, H_1 + H_2) \tag{6}$$

and

$$\left. \frac{\partial \phi^{(2)}}{\partial z} \right|_{z=H_1+H_2} = \left. \frac{\partial \phi^{(3)}}{\partial z} \right|_{z=H_1+H_2}. \tag{7}$$

We also require that a radiation condition be satisfied; that is, we must have outgoing waves at large distances from the source.

To solve Eq. (1), we perform a double Fourier transform on the variables x and y, expressing $\phi(x, y, z)$ as

$$\phi(x, y, z) = \frac{1}{(2\pi)^2} \iint_{-\infty}^{\infty} u(\eta_x, \eta_y, z) e^{i(\eta_x x + \eta_y y)} d\eta_x \, d\eta_y, \tag{8}$$

with

$$u(\eta_x, \eta_y, z) = \iint_{-\infty}^{\infty} \phi(x, y, z)e^{-i(\eta_x x + \eta_y y)} dx \, dy.$$

Substituting Eq. (8) in Eq. (1), we obtain the equation for $u(\eta_x, \eta_y, z)$,

$$\frac{d^2 u}{dz^2} + [k^2(z) - \eta^2] u = -\delta(z - z_0), \tag{9}$$

4

where $k(z) = \omega/c(z)$ and $\eta^2 = \eta_x^2 + \eta_y^2$. We note that $u(z)$ must satisfy the boundary conditions given by Eqs. (3) through (7). To solve Eq. (9), we expand $u(z)$ in the complete set of eigenfunctions $u_n(z)$ which satisfy the equation

$$\frac{d^2 u_n}{dz^2} + [k^2(z) - k_n^2] u_n = 0 \tag{10}$$

and the boundary conditions Eqs. (3) through (7), and in addition we require that $u_n(z)$ be bounded as $z \to \infty$. It can be shown that the eigenfunctions $u_n(z)$ form a complete orthonormal set satisfying the orthonormality relation

$$\int_{-\infty}^{\infty} \rho \, u_n(z) u_m(z) \, dz = \delta_{nm},$$

where the density ρ takes its appropriate value in each layer. The spectrum of eigenvalues consists of a discrete part and a continuous part, the discrete eigenvalues occurring in the interval

$$\frac{\omega}{c_3} < k_n < \max \left[\frac{\omega}{c_1(z)} \text{ or } \frac{\omega}{c_2(z)} \right],$$

provided that $\omega/c_3 < \max [\omega/c_1(z) \text{ or } \omega/c_2(z)]$. If the latter inequality does not hold, the eigenvalue spectrum is continuous. In the present problem we consider only the discrete eigenvalues, since the continuous spectrum makes a negligible contribution except at very short ranges.

Proceeding with the solution of Eq. (9), we expand $u(\eta_x, \eta_y, z)$ in the $u_n(z)$'s,

$$u(\eta_x, \eta_y, z) = \sum_n a_n(\eta_x, \eta_y) \, u_n(z),$$

and substitute this expansion in Eq. (9). Then using Eq. (10), multiplying the resulting equation by $\rho(z) u_m(z)$, and integrating over z from 0 to ∞, we find

$$a_n = \frac{\rho(z_0) u_n(z_0)}{\eta^2 - k_n^2}.$$

Thus

$$u(\eta_x, \eta_y, z) = \rho(z_0) \sum_n \frac{u_n(z_0) u_n(z)}{\eta^2 - k_n^2},$$

and thus

$$\phi(x, y, z) = \frac{\rho(z_0)}{(2\pi)^2} \iint_{-\infty}^{\infty} \sum_n \frac{u_n(z_0) u_n(z)}{\eta^2 - k_n^2} e^{i(\eta_x x + \eta_y y)} \, d\eta_x d\eta_y. \tag{11}$$

Since the problem is cylindrically symmetric, we can transform to cylindrical coordinates (r, θ, z) and, remembering the radiation condition, perform the integration in Eq. (11), finally obtaining

$$\phi(r, z) = \frac{i}{4} \rho(z_0) \sum_n u_n(z_0) u_n(z) \, H_0^{(1)}(k_n r), \tag{12}$$

5

where $H_0^{(1)}$ is the zero-order Hankel function of the first kind. At sufficiently long range we can use the asymptotic form of the Hankel function

$$H_0^{(1)}(k_n r) \sim \left[\frac{2}{\pi k_n r}\right]^{1/2} e^{i(k_n r - \pi/4)}$$

and, restoring the time dependence, obtain for the velocity potential

$$\phi(r, z) e^{-i\omega t} = i\rho(z_0) \left[\frac{1}{8\pi r}\right]^{1/2} e^{-i\pi/4} \sum_n \frac{u_n(z_0) u_n(z)}{k_n^{1/2}} e^{i(k_n r - \omega t)} \tag{13}$$

The solution shows that the sound is propagated in the normal modes of the duct, each mode suffering cylindrical spreading and having a characteristic phase velocity ω/k_n, a variation with source depth proportional to $u_n(z_0)$, and a variation with receiver depth proportional to $u_n(z)$. If the source emits a pulse, it can be shown from Eq. (2) that each mode is propagated with a group velocity

$$U_n = \frac{\partial \omega}{\partial k_n}. \tag{14}$$

The modes, which overlap at the source, then tend to separate at increasing range.

The normal-mode method has reduced the problem to the solution of Eq. (10) with the boundary conditions, an eigenvalue problem in one variable. The solution yields the eigenfunctions $u_n(z)$ and the eigenvalues k_n, which are then used in Eq. (13) to obtain the sound field.

Three-Fluid Model with Attenuation Included

In the preceding treatment of the three-fluid model we have assumed no loss mechanisms in any of the media. Attenuation due to the water layer itself is small at the frequencies of interest and the propagation distances possible in shallow water, so we neglect it and confine our attention to bottom loss and loss due to scattering at the boundaries, which are generally irregular.

Let the bottom be characterized by complex wavenumbers whose real parts are $\omega/c_2(z)$ and ω/c_3 and whose imaginary parts are ϵ_2 and ϵ_3, the latter assumed to be independent of range and depth. The imaginary parts ϵ_2 and ϵ_3 are the plane-wave attenuation coefficients in the second and third layers. The eigenfunctions $u_n(z)$ and the eigenvalues k_n then will be complex; their complex conjugates will be denoted by $\bar{u}_n(z)$ and $\bar{k}_n$. We have that

$$\frac{d^2 u_n^{(1)}}{dz^2} + \left[\left[\frac{\omega}{c_1(z)}\right]^2 - k_n^2\right] u_n^{(1)} = 0 \text{ for } 0 \leqslant z \leqslant H_1, \tag{15}$$

$$\frac{d^2 u_n^{(2)}}{dz^2} + \left[\left[\frac{\omega}{c_2(z)} + i\epsilon_2\right]^2 - k_n^2\right] u_n^{(2)} = 0 \text{ for } H_1 \leqslant z \leqslant H_1 + H_2, \tag{16}$$

and

$$\frac{d^2 u_n^{(3)}}{dz^2} + \left[\left[\frac{\omega}{c_3} + i\epsilon_3\right]^2 - k_n^2\right] u_n^{(3)} = 0 \text{ for } H_1 + H_2 \leqslant z < \infty, \tag{17}$$

6

where $u_n^{(1)}(z)$, $u_n^{(2)}(z)$, and $u_n^{(3)}(z)$ denote the eigenfunctions in the first, second, and third layers respectively. Multiplying Eq. (15) by $\bar{u}_n(z)$ and subtracting from its complex conjugate, we obtain

$$\bar{u}_n^{(1)} \frac{d^2 u_n^{(1)}}{dz^2} - u_n^{(1)} \frac{d^2 \bar{u}_n^{(1)}}{dz^2} - \left(k_n^2 - \bar{k}_n^2\right) \bar{u}_n^{(1)} u_n^{(1)} = 0. \tag{18}$$

Integrating Eq. (25) from 0 to H_1 and performing one partial integration yields

$$\left[\bar{u}_n^{(1)} \frac{du_n^{(1)}}{dz} - u_n^{(1)} \frac{d\bar{u}_n^{(1)}}{dz}\right]_0^{H_1} - \left(k_n^2 - \bar{k}_n^2\right) \int_0^{H_1} |u_n^{(1)}|^2 \, dz = 0. \tag{19}$$

Performing similar operations on Eqs. (16) and (17) gives

$$\left[\bar{u}_n^{(2)} \frac{du_n^{(2)}}{dz} - u_n^{(2)} \frac{d\bar{u}_n^{(2)}}{dz}\right]_{H_1}^{H_1+H_2} - \left(k_n^2 - \bar{k}_n^2\right) \int_{H_1}^{H_1+H_2} |u_n^{(2)}|^2 \, dz$$
$$= -4i\epsilon_2\omega \int_{H_1}^{H_1+H_2} \frac{|u_n^{(2)}|^2}{c_2(z)} \, dz \tag{20}$$

and

$$\left[\bar{u}_n^{(3)} \frac{du_n^{(3)}}{dz} - u_n^{(3)} \frac{d\bar{u}_n^{(3)}}{dz}\right]_{H_1+H_2}^{\infty} - \left(k_n^2 - \bar{k}_n^2\right) \int_{H_1+H_2}^{\infty} |u_n^{(3)}|^2 \, dz$$
$$= -\frac{4i\epsilon_3\omega}{c_3} \int_{H_1+H_2}^{\infty} |u_n^{(3)}|^2 \, dz. \tag{21}$$

Letting $k_n = \kappa_n + i\delta_n$, multiplying Eqs. (19), (20), and (21) by ρ_1, ρ_2, and ρ_3 respectively, and adding, we obtain after some manipulation

$$\delta_n = \epsilon_2 \gamma_n^{(2)} + \epsilon_3 \gamma_n^{(3)} + S_0 + S_1 + S_2, \tag{22}$$

with

$$\gamma_n^{(2)} = \frac{\rho_2\omega}{\kappa_n} \int_{H_1}^{H_1+H_2} \frac{|u_n^{(2)}|^2}{c_2(z)} \, dz / N^2, \tag{23}$$

$$\gamma_n^{(3)} = \frac{\rho_3\omega}{\kappa_n c_3} \int_{H_1+H_2}^{\infty} |u_n^{(3)}|^2 \, dz / N^2, \tag{24}$$

$$S_0 = \rho_1 \left[u_n^{(1)} \frac{d\bar{u}_n^{(1)}}{dz} - \bar{u}_n^{(1)} \frac{du_n^{(1)}}{dz}\right]_{z=0} / N^2, \tag{25}$$

$$S_1 = \frac{\rho_1 \left[\bar{u}_n^{(1)} \frac{du_n^{(1)}}{dz} - u_n^{(1)} \frac{d\bar{u}_n^{(1)}}{dz}\right]_{z=H_1} - \rho_2 \left[\bar{u}_n^{(2)} \frac{du_n^{(2)}}{dz} - u_n^{(2)} \frac{d\bar{u}_n^{(2)}}{dz}\right]_{z=H_1}}{N^2}, \tag{26}$$

$$S_2 = \frac{\rho_2 \left[\bar{u}_n^{(2)} \frac{du_n^{(2)}}{dz} - u_n^{(2)} \frac{d\bar{u}_n^{(2)}}{dz}\right]_{z=H_1+H_2} - \rho_3 \left[\bar{u}_n^{(3)} \frac{du_n^{(3)}}{dz} - u_n^{(3)} \frac{d\bar{u}_n^{(3)}}{dz}\right]_{z=H_1+H_2}}{N^2}, \tag{27}$$

7

and

$$N^2 = \rho_1 \int_0^{H_1} |u_n^{(1)}|^2 \, dz + \rho_2 \int_{H_1}^{H_1 + H_2} |u_n^{(2)}|^2 \, dz + \rho_3 \int_{H_1 + H_2}^{\infty} |u_n^{(3)}|^2 \, dz, \qquad (28)$$

where we have assumed that $u_n^{(3)} \to 0$ and $\dfrac{du_n^{(3)}}{dz} \to 0$ as $z \to \infty$.

The first and second terms in Eq. (22) are the contributions of loss in the second and third layers to the mode attenuation coefficient δ_n. The last three terms in Eq. (22) vanish if the usual boundary conditions hold, and it will be shown in a later section how these terms can be used to obtain the loss when the boundaries are randomly rough. If the usual boundary conditions hold and if $\epsilon_2 \ll \omega/c_2(z)$ and $\epsilon_3 \ll \omega/c_3$, we can use as an approximation the $u_n(z)$'s and the k_n's calculated from the ideal case. This is a good approximation for most shallow-water areas and allows the straightforward calculation of δ_n if ϵ_2 and ϵ_3 are known.

Solid Bottom Model in the Ideal Case of No Attenuation

The solid-bottom model is exactly the same as the three-fluid model (Fig. 1) except that the semi-infinite fluid layer in the latter is replaced by a semi-infinite isotropic solid layer with compressional-wave speed c_{3c}, shear-wave speed c_{3s}, and density ρ_3, all constants.

Following Ewing, Jardetzky, and Press [3], we will characterize the acoustic field in the solid layer by velocity potentials $\phi^{(3)}$ and $\psi^{(3)}$ satisfying the equations

$$\nabla^2 \phi^{(3)} + \left(\frac{\omega}{c_{3c}}\right)^2 \phi^{(3)} = 0$$

and

$$\nabla^2 \psi^{(3)} + \left(\frac{\omega}{c_{3s}}\right)^2 \psi^{(3)} = 0,$$

where we have assumed cylindrical symmetry and will be working in cylindrical coordinates. In the two fluid layers Eq. (1) and the boundary conditions given by Eqs. (3), (4), and (5) still hold. At the boundary $z = H_1 + H_2$, between the second fluid and the solid, we require that the normal component of the displacement (or velocity) and the two components of the stress be continuous.

To solve the problem, we use the same procedure as in the fluid case, transforming the radial variable and expanding $\phi^{(3)}$ and $\psi^{(3)}$ in terms of the set of eigenfunctions $u_n^{(3)}$ and $v_n^{(3)}$ respectively, defined by the equations

$$\frac{d^2 u_n^{(3)}}{dz^2} + \left[\left(\frac{\omega}{c_{3c}}\right)^2 - k_n^2\right] u_n^{(3)} = 0 \qquad (29)$$

and

$$\frac{d^2 v_n^{(3)}}{dz^2} + \left[\left(\frac{\omega}{c_{3s}}\right)^2 - k_n^2\right] v_n^{(3)} = 0. \qquad (30)$$

Equation (10) still holds for $u_n^{(1)}$, and $u_n^{(2)}$, as do the boundary conditions Eqs. (4), (5), and (6). At the boundary $z = H_1 + H_2$ the continuity of displacement gives

8

$$\frac{du_n^{(2)}}{dz} = \frac{du_n^{(3)}}{dz} + \frac{d^2 v_n^{(3)}}{dz^2} + \left(\frac{\omega}{c_{3s}}\right)^2 v_n^{(3)}, \tag{31}$$

the continuity of the normal component of stress gives

$$\rho_2 u_n^{(2)} = \rho_3 u_n^{(3)} - 2\rho_3 \left(\frac{c_{3s}}{\omega}\right)^2 \left[\frac{d^2 u_n^{(3)}}{dz^2} + \left(\frac{\omega}{c_{3c}}\right)^2 u_n^{(3)} + \frac{d^3 v_n^{(3)}}{dz^3} + \left(\frac{\omega}{c_{3s}}\right)^2 \frac{dv_n^{(3)}}{dz}\right], \tag{32}$$

and the continuity of the tangential stress gives

$$0 = 2\frac{du_n^{(3)}}{dz} + 2\frac{d^2 v_n^{(3)}}{dz^2} + \left(\frac{\omega}{c_{3s}}\right)^2 v_n^{(3)}, \tag{33}$$

since the tangential stress in the fluid vanishes.

Equations (10), (29), and (30) together with the boundary conditions Eqs. (3), (4), (5), (31), (32), and (33) and the radiation condition define an eigenvalue problem. The discrete eigenvalues occur in the interval

$$\frac{\omega}{c_{3s}} < k_n \text{ for } n = 1$$

and

$$\frac{\omega}{c_{3s}} < k_n < \max\left[\frac{\omega}{c_1(z)} \text{ or } \frac{\omega}{c_2(z)}\right] \text{for } n > 1,$$

where we have assumed throughout that $c_{3s} > \min[c_1(z) \text{ or } c_2(z)]$. The eigenfunctions are normalized according to the condition

$$\rho_1 \int_0^{H_1} u_n^{(1)} u_m^{(1)} \, dz + \rho_2 \int_{H_1}^{H_1+H_2} u_n^{(2)} u_m^{(2)} \, dz$$

$$+ \rho_3 \int_{H_1+H_2}^{\infty} [q_n q_m + r_n v_m^{(3)} + r_m v_n^{(3)}] \, dz = \delta_{nm}, \tag{34}$$

where

$$q_n = u_n^{(3)} + \frac{d v_3^{(3)}}{dz}$$

and

$$r_n = \frac{du_n^{(3)}}{dz} + \frac{d^2 v_n^{(3)}}{dz^2} + \frac{1}{2}\left(\frac{\omega}{c_{3s}}\right)^2 v_n^{(3)}.$$

The velocity potential in either of the fluid layers, in which we are primarily interested, is still given by Eq. (12) or at sufficiently long range by Eq. (13). The group velocity is still given by Eq. (14).

Solid-Bottom Model with Attenuation Included

The loss mechanisms can be introduced into the solid model by the methods used in the three-fluid case. As before, we assume that the wavenumbers of the bottom layers are complex. Let ϵ_2 be the imaginary part of the wavenumber in the second layer whose real part is $\omega/c_2(z)$. In the third layer let the compressional wavenumber have real part ω/c_{3c} and imaginary part ϵ_{3c} and the shear wavenumber have real part ω/c_{3s} and imaginary part ϵ_{3s}. Then, by the same method used before, we can derive an expression for the mode attenuation coefficient δ_n. We find that

$$\delta_n = \epsilon_2 \gamma_n^{(2)} + \epsilon_{3c}\gamma_n^{(3c)} + \epsilon_{3s}\gamma_n^{(3s)} + S_0 + S_1 + S_2,$$

where $\gamma_n^{(2)}$ is given by Eq. (3), as in the three-fluid case. The attenuation ratios $\gamma_n^{(3c)}$ and $\gamma_n^{(3s)}$ are

$$\gamma_n^{(3c)} = \rho_3 \frac{\omega}{c_{3c}} \frac{\left[2\kappa_n^2 - \left[\frac{\omega}{c_{3s}}\right]^2\right]^2}{2\kappa_n\left[\frac{\omega}{c_{3s}}\right]^4 \left[\kappa_n^2 - \left[\frac{\omega}{c_{3c}}\right]^2\right]^{3/2}} \left[\frac{du_n^{(2)}}{dz}\right]_{z=H_1+H_2} \tag{35}$$

and

$$\gamma_n^{(3s)} = \rho_2 \left\{ \frac{2\kappa_n}{\left[\frac{\omega}{c_{3s}}\right]^5} \frac{\left[4\kappa_n^2 - 3\left[\frac{\omega}{c_{3s}}\right]^2\right]}{\left[\kappa_n^2 - \left[\frac{\omega}{c_{3s}}\right]^2\right]^{1/2}} \right.$$

$$\left. - \frac{4\kappa_n\left[2\kappa_n^2 - \left[\frac{\omega}{c_{3s}}\right]^2\right]}{\left[\frac{\omega}{c_{3s}}\right]^5 \left[\kappa_n^2 - \left[\frac{\omega}{c_{3c}}\right]^2\right]^{1/2}} \right\} \left[\frac{du_n^{(2)}}{dz}\right]_{z=H_1+H_2}. \tag{36}$$

The terms S_0 and S_1 are given by Eqs. (25) and (26) respectively, except that N^2 is replaced by the normalization expression for the solid case, that is, Eq. (34) with $n = m$. Roughness at the fluid solid interface has not been considered; thus we set $S_2 = 0$. As before, we approximate Eqs. (23), (35), (36), (25), and (26) by using the unperturbed values of $u_n^{(1)}$, $u_n^{(2)}$, $u_n^{(3)}$, $v_n^{(3)}$, and k_n, which enables us to calculate the mode attenuation coefficients δ_n if ϵ_2, ϵ_{3c}, and ϵ_{3s} are known.

Boundary Roughness

In this section we consider those effects on acoustic propagation in shallow water due to the random roughness of the boundaries. Essentially, rough boundaries will cause a decay in the mean value of the acoustic field as a function of range. The effects of boundary roughness can be included in a normal-mode model by using appropriate boundary conditions on the mean field. These boundary conditions characterize the roughness and will depend on the rms height of the roughness and the surface-wave spectrum which characterizes the horizontal

variation of the surface statistics. One can then solve the wave equation for the mean field with these new boundary conditions.

In what follows we will outline the derivation of a general form of rough-boundary conditions. More detail is given in two recent papers [4,5]. That is, we will consider the boundary conditions associated with a randomly rough two-fluid interface. In the limit of the density of the second fluid going to zero, such a class of boundary conditions also includes the pressure-release condition.

To be reasonably assured that the derived boundary conditions will give plausible results in a waveguide, we will first use these conditions to derive reflection and transmission coefficients at a randomly rough two-fluid interface. We will then show that in the Kirchhoff approximation they reduce to those obtained by earlier investigators. We will present calculated results for the reflection of sound from an ocean surface described by the Pierson-Moskowitz model of a fully developed sea. We will show that in this example the reflection coefficient is a function of wind speed and wind direction. This is not the case in the Kirchhoff approximation.

Next we will apply these boundary conditions to the waveguide problem. The result is that the wavenumbers associated with each normal mode (of a lossless medium) become complex. The imaginary part of each wavenumber, as we discussed in the section titled "Signal Field," is the attenuation coefficient due to scattering associated with that particular normal mode. At no point in the derivation is any ray approximation made; the formalism is strictly wave-theory analysis. We will present calculated results for various ocean conditions where sound-speed profile, wind speed, and wind direction are varied.

Boundary Conditions for a Randomly-Rough Two-Fluid Interface

Figure 2 displays the two-fluid rough surface geometry. The fields are described by velocity potentials v_1 and v_2 in the regions with sound speeds c_1 and c_2 respectively and densities ρ_1 and ρ_2 respectively. The rough surface is described by the random function $\alpha(\vec{r})$ with mean zero where $\vec{r} = (x,y)$. The rms value of α and its transverse gradient are taken to be
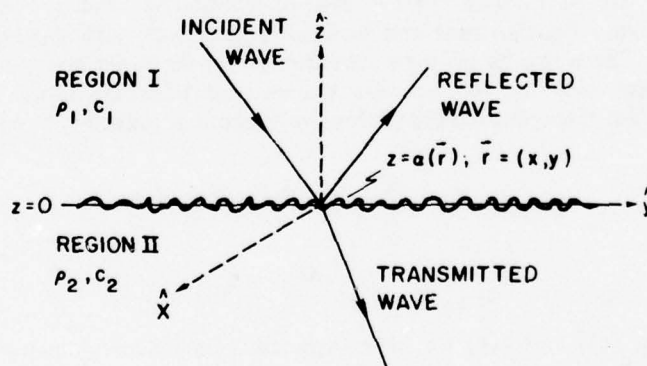

Fig. 2 — Geometry of the randomly rough
two-fluid interface

11

small as compared to the acoustic wavelength. We require that the pressure and the normal component of the particle velocity be continuous across the interface. Therefore we must have

$$\rho_1 v_1 (\vec{r},z)\big|_{z=\alpha(\vec{r})} = \rho_2 v_2 (\vec{r},z)\big|_{z=\alpha(\vec{r})} \tag{37}$$

and

$$\frac{\partial v_1}{\partial n}\bigg|_{z=\alpha(\vec{r})} = \frac{\partial v_2}{\partial n}\bigg|_{z=\alpha(\vec{r})} , \tag{38}$$

where $\partial/\partial n$ is the local partial derivative normal to the interface. With α taken to be small, we can expand Eqs. (37) and (38) in a Taylor series about the plane $z = 0$. We retain terms to order α^2. Next, following the perturbation method of Bass [6] (originally developed for a pressure-release surface), we decompose the velocity potentials into average ($<v_i>$) and stochastic (w_i) parts: $v_i = <v_i> + w_i$, $i = 1, 2$. After some algebra and taking averages, we obtain two sets of boundary conditions at the plane $z = 0$:

$$\rho_1 <v_1> - \rho_2 <v_2> = f_1 (w_1, w_2, <v_1>, <v_2>), \tag{39}$$

$$\frac{\partial <v_1>}{\partial z} - \frac{\partial <v_2>}{\partial z} = f_2 (w_1, w_2, <v_1>, <v_2>) \tag{40}$$

and

$$\rho_1 w_1 - \rho_2 w_2 = g_1 (<v_1>, <v_2>), \tag{41}$$

$$\frac{\partial w_1}{\partial z} - \frac{\partial w_2}{\partial z} = g_2 (<v_1>, <v_2>). \tag{42}$$

The functions f_1, f_2, g_1, and g_2, which are complicated functions of the fields and their derivatives, are presented elsewhere [4] and are not reproduced here. Note, though, that f_1 and f_2 are of the order $<\alpha^2>$, which indicates that the mean perturbed field will differ from the unperturbed field by order $<\alpha^2>$. However the functions g_1 and g_2 are of order α. Therefore, if we use the unperturbed potentials on the right-hand sides of Eqs. (41) and (42), these equations will still be valid to order α and, in addition, g_1 and g_2 will now be known quantities. We then use a Fourier-transform method to solve Eqs. (41) and (42) for w_1 and w_2 on the plane $z = 0$. These results are then substituted into the functions f_1 and f_2 so that the right-hand sides of Eqs. (39) and (40) are now known quantities. Equations (39) and (40) are solved by assuming that the acoustic field consists of incoming, reflected, and transmitted plane waves:

$$<v_1> = e^{i\vec{k_\perp} \cdot \vec{r}} [e^{-ik_{1z}z} + Re^{ik_{1z}z}] \tag{43}$$

and

$$<v_2> = Te^{i(\vec{k_\perp} \cdot \vec{r} - k_{2z}z)} \tag{44}$$

In writing down Eqs. (43) and (44) we have assumed a time dependence of $e^{-i\omega t}$. In Eqs. (43) and (44) R and T are the plane-wave reflection and transmission coefficients respectively. The wave vectors $\vec{k_i}$ are represented by the vectors $(k_\perp, k_{iz})$, with $\vec{k_\perp}$ being the transverse component of the wave vector. The component $\vec{k_\perp}$ is the same in both media, because it can

be shown that Snell's law must still be valid for the mean perturbed field. After we substitute Eqs. (43) and (44) into Eqs. (39) and (40), we obtain rather complicated expressions for the reflection and transmission coefficients. We will present some simpler results obtained by taking certain limits. The generalized results are given in Ref. 4.

In the limit of the Kirchhoff approximation the complexity of the mathematics is greatly reduced. The Kirchhoff approximation assumes the "the field near every region of the surface is essentially what it would have been if the surface had been flat with a slope equal to that of the irregular surface at the point in question" [7]. We obtain this limit by taking the surface correlation function to be large with respect to the acoustic wavelength (see Section II of Ref. 4). In this limit the reflection and transmission coefficients are

$$R = R_0 \left(1 - 2 k_{1z}^2 <\alpha^2> \right) \tag{45}$$

and

$$T = T_0 \left[1 - \frac{1}{2} (k_{1z} - k_{2z})^2 <\alpha^2> \right], \tag{46}$$

where R_0 and T_0 are the Rayleigh reflection and transmission coefficients respectively.

If we are considering a pressure-release surface, then $R_0 = -1$ and therefore

$$R = -1 + 2 k_{1z}^2 <\alpha^2>.$$

This result is identical to order $<\alpha^2>$ to that obtained by Eckart [8] using the Kirchhoff approximation. Beckmann and Spizzichino [9] have shown that the reflection results from a rough interface separating two media can be obtained by assuming that the Rayleigh reflection coefficient is locally valid in the Kirchhoff approximation. Clay [10], using the Rayleigh reflection coefficient together with the Eckart method, obtained a coefficient identical to Eq. (45) to order $<\alpha^2>$.

Medwin and Hagy [11] used a similar procedure to derive a coherent transmission coefficient for the case in which the density of the second medium was much larger than that of the first medium. Their results and the preceding results for T are equivalent to order $<\alpha^2>$. In addition, Eq. (46) indicates that the form of the Medwin-Hagy results (at least to order $<\alpha^2>$) is valid for arbitrary density ratio and not just in the limit of high density of the second medium as they originally assumed.

Next we present some results for a non-Kirchhoff case. We consider a pressure-release surface, so that the mathematics does not obscure the actual method. We obtain the pressure-release condition by letting ρ_2 vanish. It can then be shown that Eqs. (39) and (41) reduce to

$$<v> = - <\alpha \frac{\partial w}{\partial z}>, z = 0, \tag{47}$$

and

$$w = -\alpha \frac{\partial <v>}{\partial z}, z = 0. \tag{48}$$

Equation (47) specifies that we must know the derivative of w on the surface. We have indicated that we can solve the system of Eqs. (41) and (42) using a Fourier-transform method.

13

This is accomplished by noting that the stochastic field must originate from the boundary and hence can be expressed in the plane-wave representation

$$w = \frac{1}{2\pi} \int d\vec{\xi}_\perp \, e^{i\vec{\xi}_\perp \cdot \vec{r}} \, e^{i\xi_z z} \, \tilde{w}(\vec{\xi}_\perp), \tag{49}$$

where

$$\xi_z = (k^2 - \xi_\perp^2)^{1/2}.$$

By Fourier-transforming Eq. (48), we obtain a value for $\tilde{w}$ which we can then insert into Eq. (49), from which we can then determine $\partial w/\partial z$ on the plane $z = 0$. Substituting this value into Eq. (47), we obtain, after much algebra and after taking an ensemble average,

$$<v> = \frac{<\alpha^2>}{(2\pi)^2} \int d\vec{\xi}_\perp \, d\vec{\xi}_1 \, (i\xi_z) e^{i(\vec{\xi}_\perp - \vec{\xi}_1) \cdot \vec{r}} \, P(\vec{\xi}_1) \frac{\partial <v(\vec{\xi}_\perp - \vec{\xi}_1)>}{\partial z}, \tag{50}$$

where $P(\vec{\xi}_1)$ is the Fourier transform of the autocorrelation function $N(\vec{\rho})$ of the surface, with the argument $\vec{\rho}$ being a displacement vector between two points on the surface. To lowest order the Fourier transform of the derivative of the field $<v(\vec{\xi}_\perp - \vec{\xi}_1)>$ can be shown to be $-4\pi i k_{1z} \delta^2 [\vec{k}_\perp - (\vec{\xi}_\perp - \vec{\xi}_1)]$, with δ^2 being a two-dimensional Dirac delta function. We can then carry out the integration of $\vec{\xi}_1$, and we obtain, after decomposing the field into incident and reflected parts, the pressure-release reflection coefficient

$$R = -1 + \frac{<\alpha^2> k_{1z}}{2\pi} \int d\vec{\xi}_\perp \, \xi_z \, P(\vec{k}_\perp - \vec{\xi}_\perp). \tag{51}$$

Equation (51) allows us to calculate the reflectivity as a function of the spatial properties of the surface. In the Kirchhoff approximation the mean value of the reflected field does not depend on the surface correlation properties [12]. We will present some numerical results in a later section.

Normal-Mode Attenuation Coefficients Due to Rough Boundaries

We now apply the preceding boundary-perturbation formalism to a waveguide problem [5]. That is, we would like to solve the three-fluid problem illustrated by Fig. 1, where now the boundaries at $z = 0$, $z = H_1$, and $z = H_1 + H_2$ are randomly rough. These boundaries are now given by $z = \alpha(\vec{r})$, $z = H_1 + \beta_1(\vec{r})$, and $z = H_1 + H_2 + \beta_2(\vec{r})$, where α_1, β_1, and β_2 are random functions with zero mean. We are therefore interested in solving Eq. (1) for the mean field with the boundary conditions derived in this section. Actually we need concern ourselves with only the z-dependent equation given by Eq. (9). Here $u(\eta_x, \eta_y, z)$ is the Fourier transform of $\phi(x, y, z)$, so that we really require the Fourier transforms of the boundary conditions we derived. For the ocean surface (Eq. (50)) the transformed boundary condition can be written as

$$u = i <\alpha^2> a(\vec{\eta}) \frac{\partial u}{\partial z}, \tag{52}$$

where

$$a(\vec{\eta}) = \frac{1}{2\pi} \int d\vec{\xi} \, [k^2(0) - \xi^2]^{1/2} \, P_0(\vec{\eta} - \vec{\xi}), \tag{53}$$

with P_0 being the power spectrum of the surface. At the two fluid-interface the transformed version of Eqs. (39) and (40) can be written as

14

$$\rho_1 u_1 - \rho_2 u_2 = <\beta^2> \left[b_1 u_1 + b_2 \frac{\partial u_1}{\partial z} \right] \tag{54}$$

and

$$\frac{\partial u_1}{\partial z} - \frac{\partial u_2}{\partial z} = <\beta^2> \left[d_1 u_1 + d_2 \frac{\partial u_1}{\partial z} \right], \tag{55}$$

where b_1, b_2, d_1, and d_2 are complicated functions given in Ref. 5. In deriving Eqs. (54) and (55), we have gone through the solution of Eqs. (41) and (42) in order to obtain expressions for the w's to substitute into the right-hand sides of Eqs. (39) and (40).

We now seek a solution of Eq. (9) using the eigenfunctions which satisfy Eq. (10) and the boundary conditions given by Eqs. (52), (54), and (55). With these boundary conditions the eigenvalues and eigenfunctions of Eq. (10) become complex. Rather than redo the complete formalism as a complex eigenvalue problem, we use the technique described in the subsection containing Eqs. (15) through (28) to derive the imaginary parts of the eigenvalues. The imaginary parts of the eigenvalues, as explained in that subsection, will then be the normal-mode attenuation coefficients due to boundary roughness.

For surface roughness we use Eq. (25) together with Eq. (52) and its complex conjugate. The result is

$$S_0 = \rho_1 <\alpha^2> (2k_n N^2)^{-1} \left| \frac{du_n^{(1)}}{dz} \right|^2_{z=0} \mathrm{Re} \, [a(k_n)], \tag{56}$$

where $a(k_n)$ is given by Eq. (53).

The expression for the attenuation coefficient due to bottom roughness has a more involved derivation. Essentially we substitute Eqs. (54) and (55) and their complex conjugates into Eq. (26). After a great deal of algebra we obtain

$$S_1 = <\beta_1^2> (2k_n N^2)^{-1} \left\{ [\bar{b}_1(k_n) + \rho_1 d_2(k_n)] \left[u_n^{(1)} \frac{du_n^{(1)}}{dz} \right]_{z=H_1} \right.$$
$$\left. + \rho_1 d_1(k_n) |u_n^{(1)}|^2_{z=H_1} + \bar{b}_2(k_n) \left| \frac{du_n^{(1)}}{dz} \right|^2_{z=H_1} \right\}. \tag{57}$$

At the deepest interface we can take advantage of the fact that the eigenfunctions in the last (isovelocity) layer have the analytic form $e^{-m_3 z}$, with $m_3 = [k_n^2 - (\omega/c_3)^2]^{1/2}$, so that we know that the ratio of the eigenfunction and its derivative at the interface $z = H_1 + H_2$ is simply $-m_3$. Then Eq. (27) together with Eqs. (54) and (55) and their complex conjugates yield

$$S_2 = <\beta_2^2> (2k_n N^2)^{-1} \left\{ [\bar{b}_1'(k_n) + \rho_2 d_2'(k_n)] \left[u_n^{(2)} \frac{du_n^{(2)}}{dz} \right]_{z=H_1+H_2} \right.$$
$$\left. + \rho_2 d_1'(k_n) |u_n^{(2)}|^2_{z=H_1+H_2} + \bar{b}_2'(k_n) \left| \frac{du_n^{(2)}}{dz} \right|^2_{z=H_1+H_2} \right\}, \tag{58}$$

where b_1', b_2' d_1', and d_2' are obtained from b_1, b_2 d_1, and d_2 of Ref. 5 by replacing all subscripts 1 by 2 and all subscripts 2 by 3.

15

The discussion accompanying Eqs. (45) and (46) was concerned with the Kirchhoff approximation. This approximation greatly simplifies the derived expression for the attenuation coefficients. For example the expression for the surface attenuation coefficient now becomes

$$S_0 = \rho_1 <\alpha^2> (2k_n N^2)^{-1} \left| \frac{du_n}{dz} \right|^2_{z=0} [k_1^2(0) - k_n^2]^{1/2}. \tag{59}$$

For future reference we also write down the bottom-roughness attenuation coefficient in the Kirchhoff limit for a two-layered waveguide whose bottom layer contains an isovelocity medium. This attenuation coefficient is

$$S_1 = <\beta^2> (2k_n N^2)^{-1} [u_n^{(1)}(H_1)]^2 (\rho_1/\rho_2^2) \gamma_1 (\rho_2^2 \gamma_1^2 + \rho_1^2 \gamma_2^2), \tag{60}$$

where

$$\gamma_1 = \left\{ [\omega/c_1(H_1)]^2 - k_n^2 \right\}^{1/2}$$

and

$$\gamma_2 = \left[k_n^2 - (\omega/c_2)^2 \right]^{1/2}$$

Recently we have also developed a wave-theory method [13] which analytically predicts the normal-mode attenuation coefficients in a duct bounded by surfaces whose plane-wave reflection coefficients differ by a small amount from the Rayleigh reflection coefficients. Since rough boundaries in the Kirchhoff approximation, to the order of the rms roughness, satisfy the conditions of Ref. 13, the attenuation coefficients should agree with those given above, though they were obtained by different techniques. Indeed, if the reflection coefficient given by Eq. (45) is used, the results are identical to those of Eqs. (59) and (60). Note, though, that the results presented in Eqs. (56), and (57), and (58) are the generalized coefficients in which no Kirchhoff approximation was made.

There is also some previous work with which we can compare the above Kirchhoff result. Clay [14] calculated the mode attenuation coefficients in isovelocity shallow water based on the idea that each time a ray associated with a normal mode bounces off the surface, it is decreased in amplitude by the Eckart [8,10] reflection factor. For a given normal mode the number of bounces to a certain range was calculated from a "skip distance" for a particular normal mode's ray representation.

The result given by Eqs. (59) and (60) are close to the Clay result but slightly smaller. This discrepancy can be explained by the same argument used to explain the attenuation of the acoustic field in the water column due to a lossy bottom [15]. Although the mode is attenuated as it is propagated, the boundary conditions must still be satisfied. Thus there will be a small flux of energy from the bottom through the interface to compensate for the decrease of the field in the water column, resulting in a smaller mode attenuation coefficient. When one uses just a skip-distance argument, such a compensation effect is not taken into account. If we take our result and make both boundaries pressure-release (or rigid) boundaries, then there will be no such effect, since the field must simply vanish at both pressure-release boundaries (or the derivatives must vanish at both rigid boundaries). For these cases Eqs. (59) and (60) are identical with the Clay result.

The surface and bottom normal-mode attenuations are equal for equal rms roughness in an isovelocity water channel. This can be understood from the ray analogy to the normal-

16

mode picture. For an unperturbed case the normal modes correspond to rays (that are actually plane waves) at angles less than the critical grazing angle at the bottom, that is, rays that are perfectly reflected at the surface and the bottom. For the isovelocity case the ray's angles are the same, and equal roughness at both interfaces just diminishes the amplitude of the ray upon reflection by the same amount.

Transmission-Loss Model

In the previous discussion we emphasized individual normal modes of propagation. We will now apply these results to the calculation of the signal field of a CW acoustic source. An expression for transmission loss is also obtained. In this calculation we assume that the receiver is sufficiently far from the source that only the discrete normal modes make a significant contribution to the signal field.

If a harmonic point source is operated in the range-independent medium described in the section titled "Signal Field," the acoustic field may be represented by a sum of terms, each of which corresponds to a single normal mode of propagation. At a range many acoustic wavelengths from the source the contribution of the nth normal mode to the instantaneous signal pressure is given by

$$p_n(t) = S \frac{(4\pi)^{1/2} \rho_1 u_n(\zeta_0) u_n(\zeta)}{r^{1/2} k_n^{1/2}} \cos(k_n r - \omega t - \pi/4) e^{-\delta_n r}, \tag{61}$$

where S is the rms free-field omnidirectional source level (re 1 m) and the normalized depth ζ is equal to z/H_1. The other quantities have been defined in the section titled "Signal Field."

If the acoustical parameters of the medium such as water depth, bottom type, or sound-speed profile are range dependent, the wave equation cannot be separated to obtain Eq. (9). The direct solution of the unreduced three-dimensional wave equation is considerably more difficult than is the solution of the separated equations. However, if the environmental parameters change sufficiently slowly with range, we may make the approximation that the wave equation is locally separable. By that we mean that if we want to calculate some property, such as vertical pressure distribution or attenuation coefficient, of the jth mode at some range, we may obtain a good approximation to that quantity from the constant-depth model using the environment at the point of interest. Thus the normal modes are assumed to adapt to the environment at the point of interest. Given sufficient slowness of the horizontal variation of the environment we may also assume that mode index is conserved, that is, that the modes are not coupled by the range-dependent environment [16,17]. Under conditions of uncoupled propagation, energy originally propagated in the jth mode remains in that mode until it is removed by absorption.

If these two assumptions are correct, we may [18] replace Eq. (61) by

$$p_n(t) = \frac{S(4\pi)^{1/2} \rho_1 u_n(\zeta_0) u_n'(\zeta)}{(\phi_n)^{1/2}} \cos(\phi_n - \omega t - \pi/4) e^{-\Delta_n r}, \tag{62}$$

where u_n and u_n are the eigenfunctions calculated at the source and receiver respectively, ϕ_n is the cumulative phase of the nth mode,

$$\phi_n = \int_0^r k_n(r') \, dr',$$

17

and Δ_n is the average attenuation coefficient,

$$\Delta_n = \frac{1}{r} \int_0^r \delta_n(r')\, dr'.$$

The results of an experimental test of Eq. (62) will be presented in a later section.

The total instantaneous pressure $p(t)$ at the field point (r, ζ) is obtained by summing the contributions of the N allowed modes:

$$p(t) = \sum_{n=1}^{N} p_n(t) = S(4\pi)^{1/2}\rho_1 \sum_{n=1}^{N} \frac{u_n(\zeta_0)u_n'(\zeta)}{\phi_n^{1/2}} \cos(\phi_n - \omega t - \pi/4)e^{-\Delta_n r}.$$

The rms pressure, averaged over a time $T \gg \dfrac{2\pi}{\omega}$, is

$$<p^2(t)> = S(4\pi)^{1/2}\rho_1^2 \left\{ \frac{1}{T}\int_0^T \left[\sum_{n=1}^{N} \frac{u_n(\zeta_0)u_n'(\zeta)}{\phi_n^{1/2}} \cos(\phi_n - \omega t - \pi/4)e^{-\Delta_n r} \right]^2 dt \right\}^{1/2}$$

This expression, which considers the relative phases of the individual modes, is called the coherent sum. The coherent transmission loss obtained from this expression is expressed in decibels:

$$TL = 10\log_{10}\left\{ (2\pi\rho_1^2) \left\{ \left[\sum_{n=1}^{N} \frac{u_n(\zeta_0)u_n'(\zeta)}{\phi_n^{1/2}} e^{-\Delta_n r}\cos\phi_n \right]^2 \right. \right.$$

$$\left. \left. + \left[\sum_{n=1}^{N} \frac{u_n(\zeta_0)u_n'(\zeta)}{\phi_n^{1/2}} e^{-\Delta_n r}\sin\phi_n \right]^2 \right\} \right\}. \qquad (63)$$

Loss calculated from this expression will usually exhibit rapid oscillations with range of order 10 to 20 dB due to the phase-dependent interference effects among the normal modes. Similar oscillations are observed in measured loss (Fig. 3). The details of this interference pattern are highly sensitive to the values of environmental parameters, such as water depth and sound-speed profiles in the water and bottom-sediment layers. These quantities, particularly the bottom-sediment sound-speed profiles, are not usually known with sufficient accuracy to allow detailed agreement between measured and calculated interference maxima and minima.

The interpretation of loss measurements like those in Fig. 3 often requires comparison with model calculations. If observed and calculated loss are rapidly oscillating functions of range, it is difficult to determine the quality of the agreement, particularly since we do not expect the maxima to coincide. The comparison is made easier if smooth curves, obtained by averaging out the interference effects, are used. Smooth calculated transmission-loss curves may be obtained by adding the energies of the individual modes rather than the pressures. The phase differences, which generate the interference effects, do not appear in this sum. This smoothed loss, called incoherent loss, is given by

18

$$TL = 10 \log_{10} \left\{ (2\pi\rho_1^2) \sum_{n=1}^{N} \left[\frac{u_n(\zeta_0) u_n'(\zeta)}{\phi_n^{1/2}} e^{-\Delta_n r} \right]^2 \right\}. \tag{64}$$

Loss-vs-range curves may be obtained from Eq. (64) with much less computational effort and expense, since the range increments at which the expression is evaluated may be made fairly large, whereas the increments used for Eq. (63) must be small enough to define the detailed oscillations in the interference pattern. Computation-time ratios of 10:1 are commonly encountered.
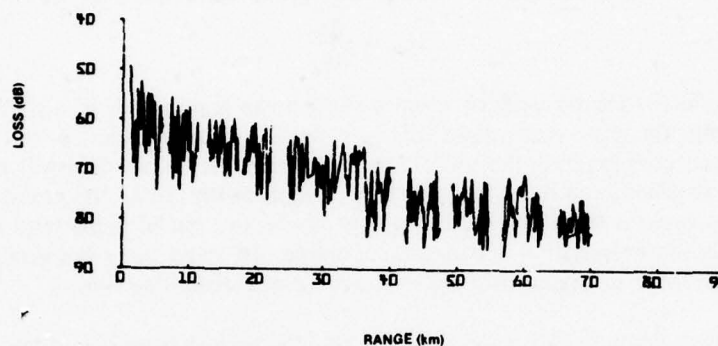
Fig. 3 — Example of measured CW transmission loss

Computer programs have been written at NRL to evaluate Eqs. (63) and (64) using normal-mode parameters calculated [19] from the fluid-subbottom and solid-subbottom models described earlier in this theory section. Loss calculated using these programs has been found to be in good agreement with loss measured over constant-depth and sloping-bottom tracks. Work is continuing to obtain additional experimental confirmation.

This loss model has been incorporated into the NAVSEA performance-prediction model for passive sonar in shallow water. This model is now under development at the Naval Undersea Center in San Diego.

EXPERIMENTAL TECHNIQUES

Requirements

The objective of the experimental program has been the validation of wave-theory models in real ocean environments. It can be shown (see Eq. (13)) that the solution to the wave equation for the NRL model results in the following expression for the pressure amplitude $P_n(r, \zeta)$ for the nth normal mode of the system:

$$P_n(r, \zeta) = \omega\rho_1^2 \left[\frac{1}{8\pi r} \right]^{1/2} \frac{u_n(\zeta_0) u_n(\zeta)}{k_n^{1/2}}, \quad 0 \leqslant \zeta \leqslant 1, \tag{65}$$

for a source of unit strength.

19

It follows that at a fixed range the modal pressure amplitude has a functional dependence on source and receiver depth given by

$$P_n(\zeta) = \psi_n u_n(\zeta_0) u_n(\zeta), \qquad (66)$$

where ψ_n is a constant of proportionality for the nth mode. This relationship is fundamental in that it defines the degree of excitation of and the relative vertical pressure amplitude distribution in each modal field.

Another intrinsic property predicted by the solution to the wave equation is the dispersion resulting from the differing propagation velocity among modes and by the frequency dependence of the modal propagation velocity. The group velocity U_n of the nth mode is

$$U_n = \frac{\partial \omega}{\partial k_n}.$$

This dispersive effect is clearly evident when a short pulse is projected in a shallow-water duct. The group velocity for any given mode will in general not be constant over the finite bandwidth of the pulse; consequently the pulse duration within the modal field will be progressively lengthened as it is propagated to increasing range. Additionally, since the group velocity at any one frequency in general will differ from mode to mode, the modal fields tend to become spatially separated as the propagation distance is increased. In some cases the modal fields from a short pulse will become separated into discrete arrivals at a distant sensor.

Another effect predicted by wave theory is the decrease in intensity of the modal fields as they are propagated away from the source. Of the several mechanisms involved in propagation loss, two are predicted as a natural consequence of the wave-theory solution. One is the geometric spreading as the field expands radially, and the other is the loss due to bottom absorption. The geometric spreading of the field in a duct of constant depth is inherent in Eq. (65). It was shown in the theory section titled "Signal Field" that if the attenuation coefficient ϵ of the bottom material is known, the associated attenuation coefficient δ_n of the modal field can be calculated from

$$\delta_n = \epsilon (\omega \rho_2 / c_2 \, k_n) \int_H^\infty [u_n^{(2)}(z)]^2 \, dz.$$

Another important loss mechanism, that due to scattering from rough boundaries, is not an inherent part of the solution to the wave equation. The relevant theory for scattering effects is given in the theory section titled "Boundary Roughness." This is a newly developed formulation and has not been addressed by the experimental validation program to date.

In summary, the experimental program has been designed to test the theory relevant to the following modal properties:

- Mode excitation,
- Vertical pressure-amplitude distribution of the modal fields,
- Dispersion, and
- Attenuation.

Another characteristic, mode phase velocities, can be obtained from the solution to the wave equation, but experimental verification of this property has not been attempted. All of the properties listed above can be calculated for each of the individual normal modes of propagation.

Direct validation therefore requires that appropriate measurements be obtained on the discrete modes rather than on the total signal field, which is the sum of the modes.

Implementation

Since the requirement was to examine the acoustic fields of individual normal modes and since in general more that one normal mode exists at frequencies of interest, it was necessary to find a technique by which the modal fields could be resolved. As was discussed, under certain conditions the differing group velocities among modes permit modal resolution by time of arrival when short pulses are propagated over long ranges. In theory, if a duct is excited with a pulse of duration τ, the components of that pulse propagated in any pair of normal modes of the duct, having group velocities U_m and U_n, will be temporally resolved at range

$$r \geqslant \tau \ U_m \ U_n / |U_m - U_n|. \tag{67}$$

It is assumed here that the pulse length τ is not lengthened significantly by dispersion.

There is of course a practical limit to the range at which the resolved modal fields can be measured, depending on the source level, propagation loss, and background noise. In the experimental program, coherent sources having resonant frequencies f of 400, 750, and 1500 Hz were driven by short (3-cycle) gated sine-wave pulses. The mechanical Q of each of the sources was approximately 4. The projected pulses therefore were approximately 4/f seconds in duration. Although the sources were driven at maximum power (free-field source levels ranging from 196 to 203 dB re 1 μPa at 1 m), only a fraction of the projected power excited any individual modal field. This fact, coupled with the broad receiving bandwidths required (f/4), resulted in a limitation of the usable range to about 20 km. Since the group velocities have values of the order of 1500 m/s, it can be seen from Eq. (67) that $|U_m - U_n|$ must have a value of at least 900/f to achieve resolution. The received pulses however are usually lengthened considerably by dispersion, so that a larger value of $|U_m - U_n|$ is required. In most cases a value of $|U_m - U_n| = 1500/f$ was found to be sufficient. When this value is used, a modal field can be resolved when its nearest neighbor differs in group velocity by 1 m/s at 1500 Hz, 2 m/s at 750 Hz, and approximately 4 m/s at 400 Hz.

Figure 4 is an example of group velocities calculated for six modes for a location off Panama City, Florida, where the water depth was 30 m and the sound-speed profile was as shown in the inset. It can be seen that at 400 Hz the first and second modes have the required separation in group velocities, (4 m/s). Higher order modes are also adequately separated, but under the prevailing conditions they were highly attenuated and their fields could not be detected. It can also be seen that the group-velocity function for the second mode has a much higher slope at 400 Hz than the first mode has. Because of this it would be expected that the pulse duration in the field of the second mode would be longer than that in the first mode, having been lengthened to a greater degree by dispersion.

Experimental Procedures

Since the intention was to examine the individual modal fields in both depth and range, the acoustic field was sampled in depth from near the surface to near the bottom by a vertical string of hydrophones which was suspended at selected horizontal ranges from the source. Figure 5 shows the experimental geometry used in all experiments except the first. In the first
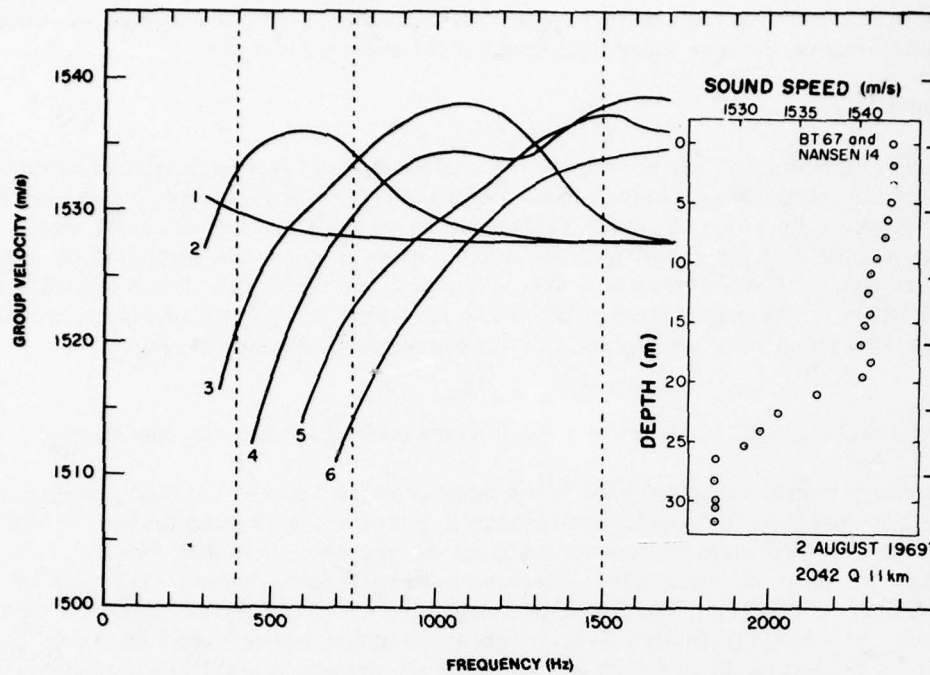
21

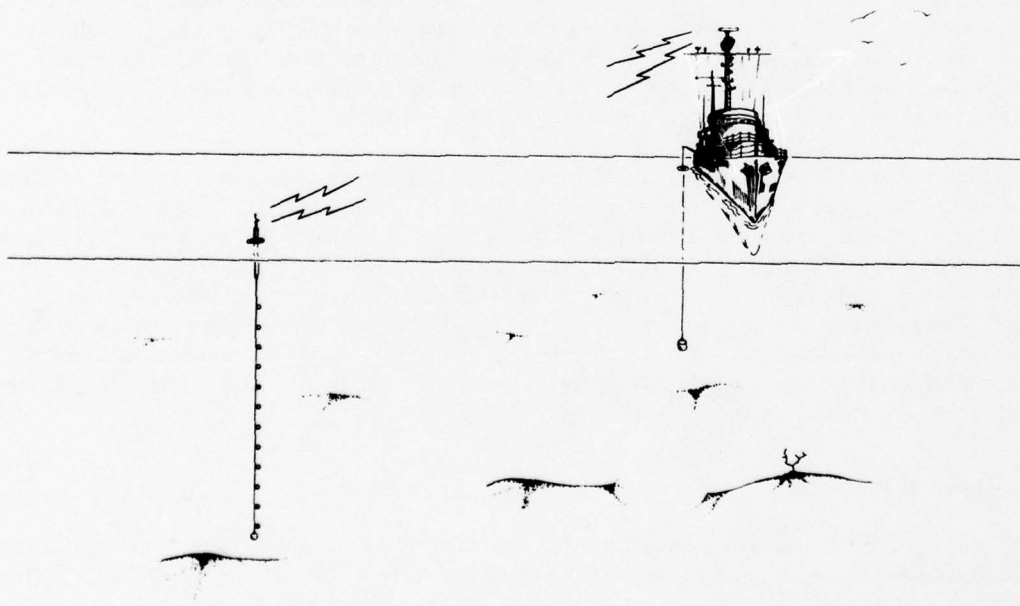Fig. 4 — Calculated group velocities for the first six modes at the Panama City location

Fig. 5 — Experimental geometry

22

experiment, the source was deployed from a fixed tower, and the hydrophone string was deployed from a ship. Three essentially omnidirectional acoustic sources were used having resonant frequencies of 400, 750, and 1500 Hz respectively. In all experiments the source could be suspended at any depth from near the surface to near the bottom.

After the first experiment the remote sensor buoy shown in Figs. 5 and 6 was developed to serve as a sensor platform. The purpose of this buoy was to permit single-ship experiments to be conducted in various ocean areas. The basic configuration of the buoy is that of a cylinder 0.38 m in diameter and 6.1 m long. The buoy floats in a vertical position with about 1.2 m of the cylinder exposed above the water's surface. A strain wire supporting a 270-kg lead ball is attached to the lower end of the buoy. Twelve hydrophones are clamped onto the strain wire at any desired spacing and connected to the buoy by individual cables. The electronics package in the buoy is shown in Fig. 7. In addition to 12 channels of radio telemetry (2-kHz bandwidth for each channel) for relaying the sensor signals to the mother ship, the buoy is provided with radio-command circuits for changing gain, for inserting calibration signals, and for turning the buoy off and on. The telemetry range is approximately 20 km, and this corresponds roughly to the maximum range at which an adequate signal-to-noise ratio exists in the acoustic signals.
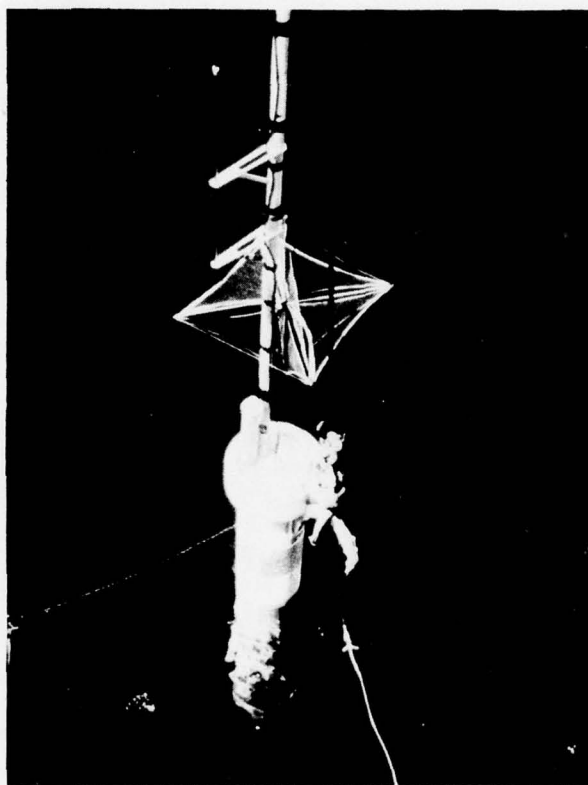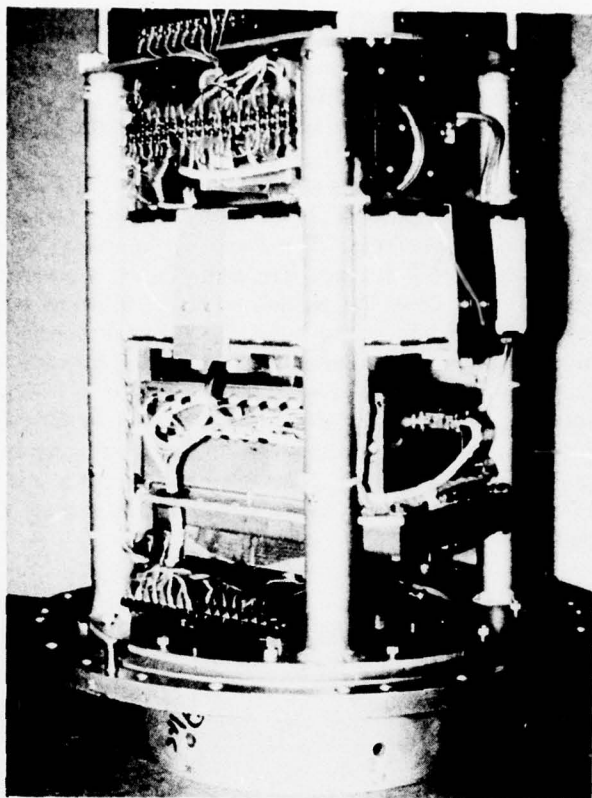

Fig. 6 — Remote sensor buoy

Fig. 7 — Electronics package of the remote sensor buoy

An example of the signal received on the buoy hydrophones is shown in Fig. 8. This oscillographic recording shows the 12 traces from the outputs of hydrophones in the vertical string, spaced at 2-m increments beginning at a 5-m depth. The water depth is 30 m. The projected pulse was 3 cycles of a gated sine wave at 750 Hz. The illustration shows that there are two principal arrivals which have been temporally separated by virtue of the differing group velocities of the modal fields. The first arrival is strongest in the lower half of the water column and has a null near the depth of the fourth hydrophone from the top. A phase reversal occurs at the null. The second arrival is predominantly in the upper half of the water column. The vertical lines in the recording are 10-ms time markers, with time progressing from left to right. The prevailing sound-speed profile is shown in Fig. 9, and the calculated group velocities and mode amplitude functions for the first six modes are shown in Figs. 10 and 11 respectively. The calculated group velocities at 750 Hz were 1507.7 and 1510.0 m/s for the first and second modes respectively. Since the range between source and receivers was 10 km for this measurement, the arrival times of the first and second modes would be expected to differ by 10 m/s, with the second mode arriving first. The close agreement between the predicted properties (vertical phase and amplitude distribution and arrival times) and those observed in Fig. 8 was strongly indicative that the observed signals corresponded to those propagated via the second and first normal modes of the duct. Although the calculated group veloci-

24

Fig. 8 — An oscillographic recording of the outputs of 12 hydrophones vertically distributed in the water column. Time progresses from left to right.
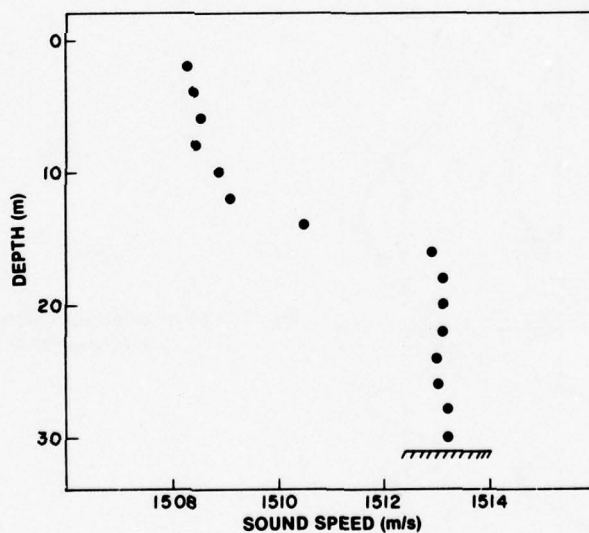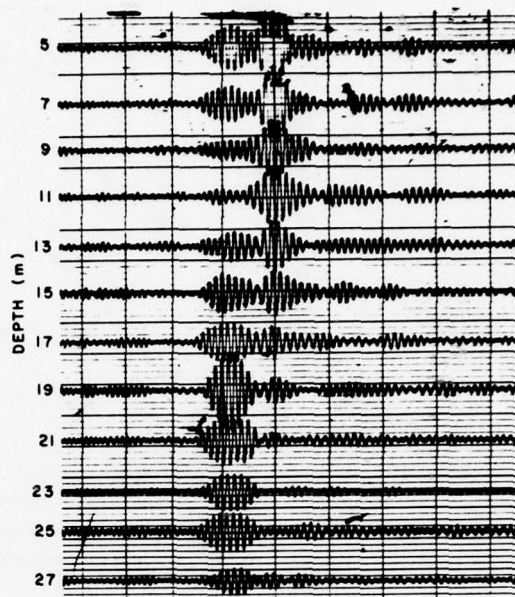

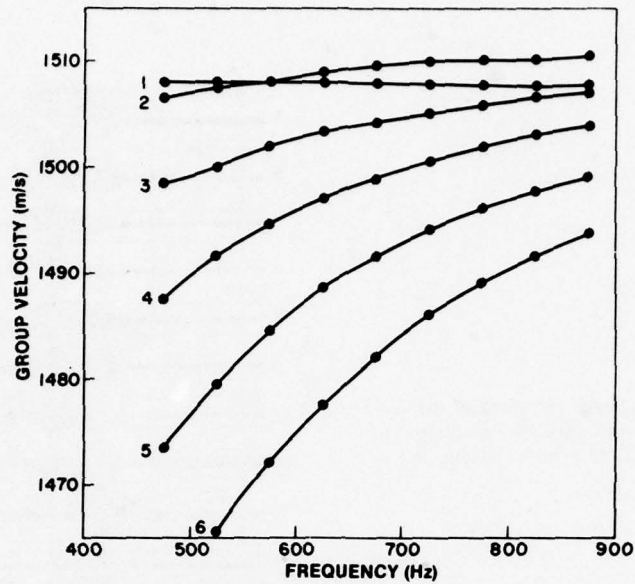Fig. 9 — A measured sound-speed profile

Fig. 10 — Group velocities for the first six modes, calculated using
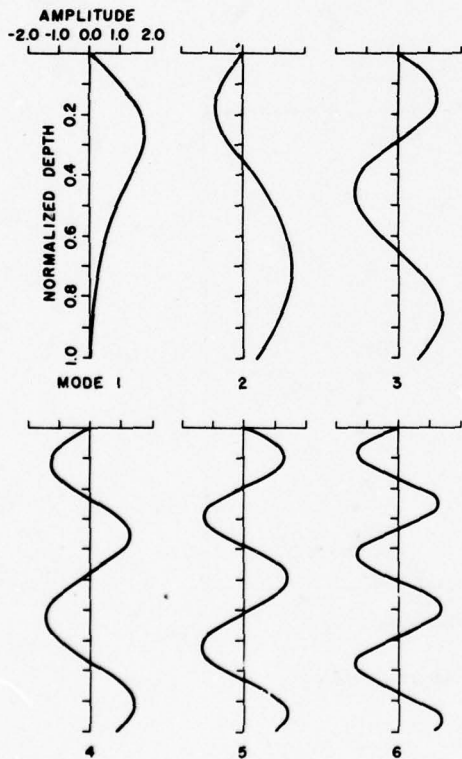the sound-speed profile of Fig. 9

Fig. 11 — Mode amplitude functions, calculated using the
sound-speed profile of Fig. 9

26

ties indicated that third and higher order modes should also be resolved, no modes of higher order than the second are identifiable in the illustrated signals, probably because they were more highly attenuated and were lost in the noise.

From data of the type shown in Fig. 8 it is possible to measure the relative strengths of the modal fields, their vertical phase and amplitude distributions, their group velocities, and the dispersion within each field. When such measurements are made as a function of range, modal attenuation coefficients can be obtained.

When complete temporal resolution of the modal fields could not be obtained, a spatial filtering technique was used to enhance the field of one mode while tending to reject all others. To do this, the outputs of the 12 hydrophones were combined in an appropriate summing network in which selected polarities and weighting factors could be introduced into each channel. The orthogonal property of the modes permits selection of channel polarities and weighting factors to produce a preferential response to a selected mode. In the experiments reported here, the outputs of the 12 hydrophones were combined in three separate summing networks. The response of each channel was adjusted in each network to be proportional to the value of and matched in polarity to the selected mode amplitude function at a corresponding depth. The three networks were matched in this manner to each of three modes. The output τ_n of a mode filter (summing network) in response to the field of the nth mode is

$$\tau_n = K \sum_{i=1}^{12} u_n(\zeta_i) \, p_n(\zeta_i, \zeta_0), \tag{68}$$

where K is a system gain factor. If the modal field has the vertical distribution predicted by Eq. (66), Eq. (68) can be rewritten as

$$\tau_n = K \psi_n u_n(\zeta_0) \sum_{i=1}^{12} u_n^2(\zeta_i). \tag{69}$$

The theoretical response of the filter to other than the selected mode can be calculated. The response to the mth mode of a filter matched to the nth mode is

$$\tau_n = K \sum_{i=1}^{12} u_n(\zeta_i) p_m(\zeta_i, \zeta_0). \tag{70}$$

If the mth mode has the predicted vertical distribution, Eq. (70) can be rewritten as

$$\tau_n = K \psi_m u_m(\zeta_0) \sum_{i=1}^{12} u_n(\zeta_i) \, u_m(\zeta_i). \tag{71}$$

Several sample calculations were made using Eqs. (69) and (71) with appropriate mode amplitude functions computed for prevailing sound-speed profiles. In the cases tested, the theoretical response to the unwanted mode ranged from 10 to 30 dB below the response to the selected mode. Even in theory complete rejection cannot be achieved, because of the finite sampling of the modal fields. Experimental tests with temporally resolved modes yielded rejection ratios only slightly degraded from theoretical ratios. An example of experimental results is shown in Fig. 12. The upper trace is the output of a single hydrophone when the modal fields are not temporally resolved. The next three traces are the outputs when mode filters are matched to the first, second, and third modes respectively. Filters such as this were found to be useful when examining a strong modal field which was not temporally resolved from a weak modal field.
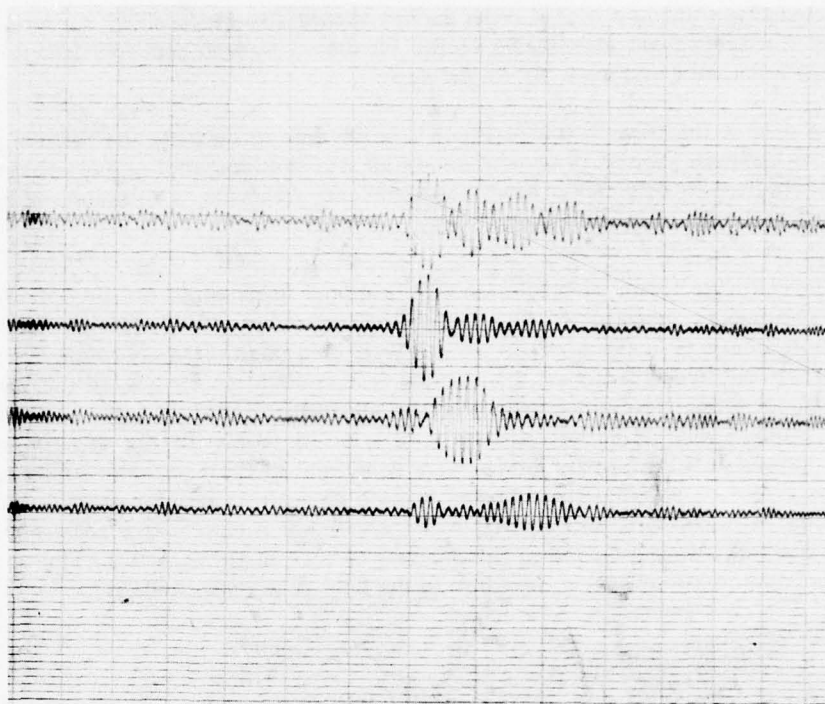
27

Fig. 12 — Example of the outputs of the mode filters

During the experiments sound-speed profiles in the water column were measured by lowering a pair of velocimeters from the surface to the bottom. The depth for each incremental reading was obtained from the marked cable. The water depth was measured using a high-frequency shallow-water depth sounder calibrated against a weighted line. Bottom cores and grab samples were obtained along each of the propagation paths.

Experimental Sites

Experiments were conducted in each of three geographical areas. The first site was an area in the Gulf of Mexico approximately 20 km offshore from Panama City, Florida. Experiments were conducted here during several intervals from July 1969 through May 1971. All experiments at this site were conducted along the same propagation path (Fig. 13), where the water depth was nearly constant 31 m above a hard sand bottom. The bottom contour along the path is shown in Fig. 14. In the first experiment at this site, described in Ref. 20, the acoustic sources were deployed from the fixed tower known as Stage I, which is a facility of the Naval Ship Research and Development Laboratory (now Naval Coastal Systems Laboratory), Panama City, the vertical hydrophone string was deployed from a ship. In subsequent experiments at this site, and at the next two sites, the sources were deployed from a ship, with the hydrophone string being suspended from the remote sensor buoy.
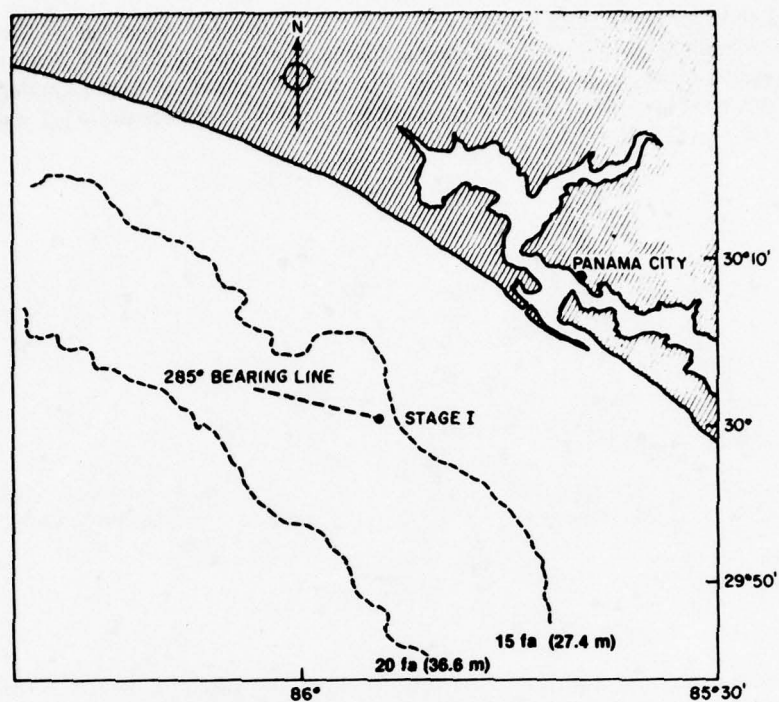
28

Fig. 13 — Operational area near Panama City, Florida.
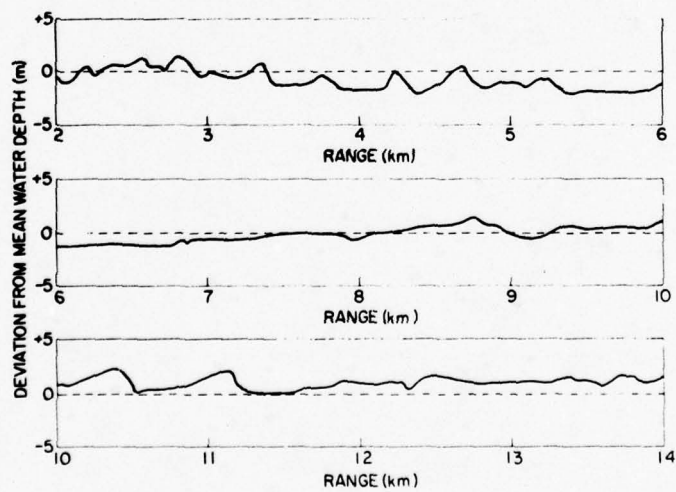Stage I is a fixed tower.

Fig. 14 — Bathymetry along the 285° bearing line from stage I (Fig. 13)

29

The second experimental area was along the southern perimeter of the Gulf of Mexico - on Campeche Bank. Experiments were conducted there during May 1972 over two propagation paths at each of two sites shown in Fig. 15. All paths had an approximately constant water depth of 32 m. The bottom was hard limestone with a thin (less than 1/2 m) covering of fine sand.
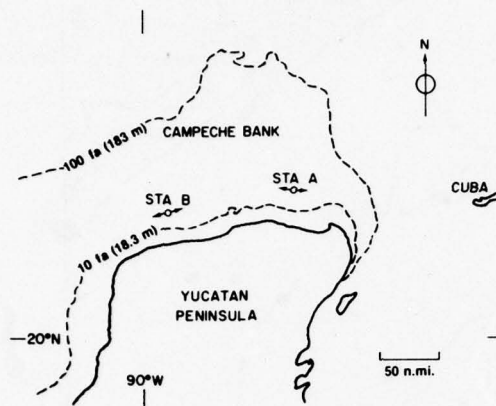

Fig. 15 — Operational area on Campeche Bank

Experiments were conducted in a third area off Daytona Beach, Florida, during November 1973. This site was selected to provide propagation paths over a sloping bottom. The location of the propagation paths is shown in Fig. 16, and the bottom contours along the paths are shown in Fig. 17. The bottom in this area is sand.
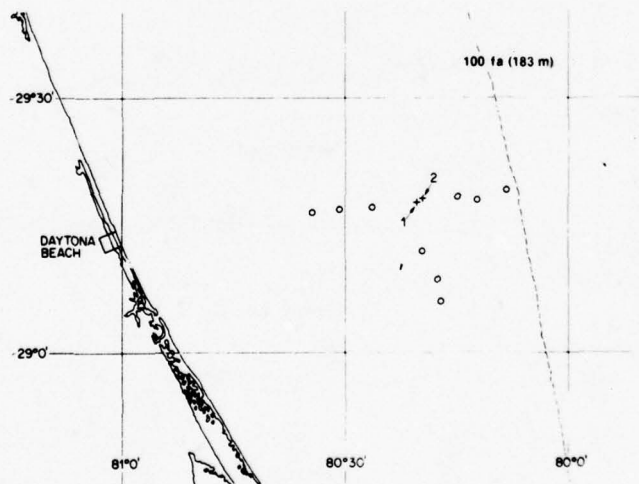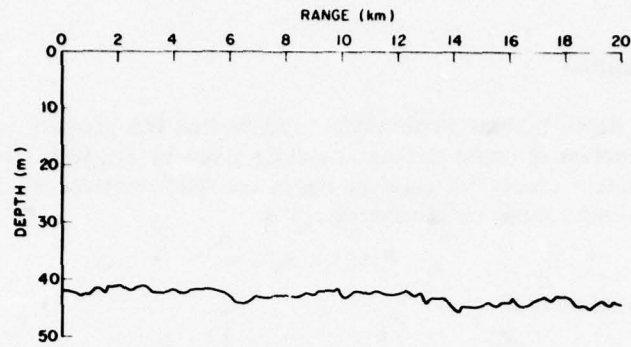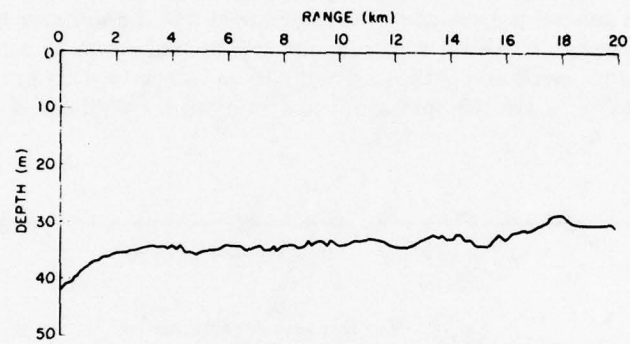

Fig. 16 — Operational area near Daytona Beach, Florida. Crosses indicate remote sensor buoy locations. Circles indicate stations that were occupied by the source ship.
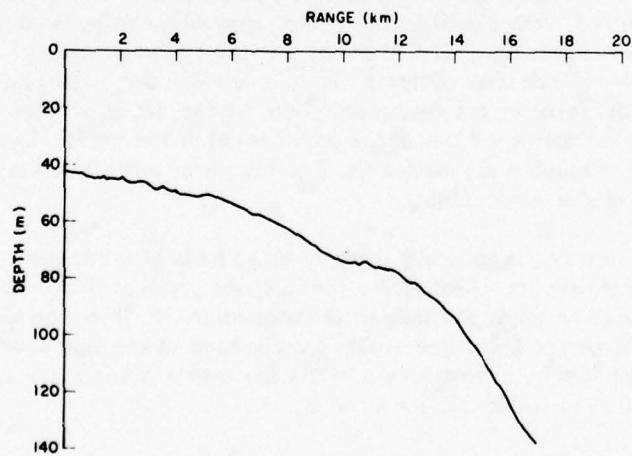
30

(a) Constant-depth track

(b) Gradually sloping track

(c) Rapidly sloping track

Fig. 17 — Bathymetry of the tracks off Daytona Beach

31

RESULTS

Modal Field Distribution

The constant-depth normal-mode model predicts that the pressure amplitude of the nth-order mode as a function of depth at range r will be given by Eq. (65). If all acoustic and environmental parameters except for receiver depth are held constant, the dependence of the pressure of the nth-order mode on receiver depth is

$$P_n(\zeta) \propto u_n(\zeta),$$

where $u_n(\zeta)$ is the solution of

$$\frac{d^2 u_n}{d\zeta^2} + H^2 \left[\frac{\omega^2}{c^2(\zeta)} - k_n^2 \right] u_n(\zeta) = 0 \qquad (72)$$

with the eigenvalue k_n. Equation (72) is Eq. (10) written in terms of the normalized depth coordinate ζ. Some general properties of the modal field distribution may be inferred from the spectrum of eigenvalues. A typical spectrum for a fluid-subbottom case is shown in Fig. 18. The subbottom sound speed is c_3, the sediment layer is assumed to have a constant sound speed c_2, and c and c_{min} are the maximum and minimum sound-speed values in the water column.
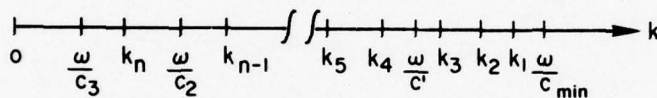

Fig. 18 — Typical eigenvalue spectrum

In this example n discrete modes are permitted. To satisfy the boundary conditions of the fluid model with normalizable eigenfunctions, the eigenvalues must be bounded by ω/c_3 and ω/c_{min}. It can be seen from Eq. (72) that at any depth ζ for which $\omega/c(\zeta) > k_j$ the jth mode tends to be an oscillatory function of depth. If $k_j > \omega/c(\zeta)$, the eigenfunction is an exponential function of depth. Thus for the case represented by Fig. 18, all n modes are exponential in the subbottom, and the first $n - 1$ modes are exponential in the bottom layer. Throughout the water layer modes 4 through n are oscillatory. The first three eigenfunctions are exponential in the high-speed part of the water column.

Since an eigenfunction is generally small in those parts of the medium in which its depth dependence is exponential, the effect of the sound-speed gradient is to confine the bulk of energy propagated in a given mode to that part of the medium in which the associated eigenfunction is oscillatory. Thus the first three modes are confined to the slow-speed part of the water column, with the confinement most severe in the first mode, since $k_1 > \omega/c(\zeta)$ over a larger part of water column than is the case for k_2 or k_3.

As the frequency of the acoustic signal increases, the eigenvalues k_j increase faster than ω. Thus the number of modes "trapped" by the gradient tends to increase with frequency, and for a given order mode the confinement generally becomes more pronounced.

32

A series of experiments [20,21] was carried out at sea to measure the pressure amplitude of individual modes as a function of depth under various environmental conditions. For all the data discussed in this section, the water depth over the propagation path was nearly constant (31 ± 2 m).

A vertical string of hydrophones was suspended from the anchored remote sensor buoy. The hydrophones were uniformly spaced and covered as much of the water column as the mechanical constraints of the system permitted. The ship then anchored at several range stations from 4 to 20 km along the 31-m isobath. At each range station coherent sources were driven by gated sinusoidal pulses at a sequence of depths. For many of the runs dispersion permitted temporal resolution of individual modal fields, as described in connection with Fig. 4. The signals from the individual hydrophones were simultaneously displayed using a multichannel oscillographic recorder. The mode order associated with one of the pulses in the sequence was determined by comparing the signal phase on adjacent channels. The signals associated with the first mode are all in phase. Those associated with the second mode show one 180° phase reversal, usually near middepth. The third mode exhibits two phase reversals.

Signal pressures were determined by comparison of the received signal amplitudes with those of a calibration signal generated by the remote sensor buoy. For each mode resolved and identified, the peak pressure in the pulse was averaged over 20 pulses, and the average was plotted as a function of receiver depth to obtain the pressure distribution of the normal mode. Agreement of calculated and measured pressure-amplitude distributions (plotted on an arbitrary amplitude scale) is shown for the first and second modes at signal frequencies of 400 Hz and 750 Hz in Fig. 19. Similar agreement between calculated and measured distributions was obtained at a signal frequency of 1500 Hz. Axis crossings of the measured pressure-amplitude distribution correspond to observed phase reversals on adjacent signal traces.

The influence of the sound-speed gradient on the low-order modes may be seen by comparing Fig. 19b (positive gradient) and Fig. 19a (negative gradient) with Fig. 19c (isovelocity profile). In the isovelocity case (Fig. 19c) the first mode is nearly symmetrically distributed about middepth. The water sound-speed gradients alter this symmetric distribution and concentrate the energy in the low-velocity portion of the water column, as can be seen in Figs. 19a and 19b.

The results discussed above were obtained at the site near Panama City, Florida, where the ocean bottom consists of hard-packed sand. Similar agreement between calculated and observed modal pressure distributions was obtained at the other two sites [13, 22], at which different bottom types (consolidated limestone and silty sand) were found.

These experiments were performed over tracks selected to have a range-independent water depth and sound-speed profile. The results of similar experiments performed over a sloping-bottom track will be presented in a later subsection.
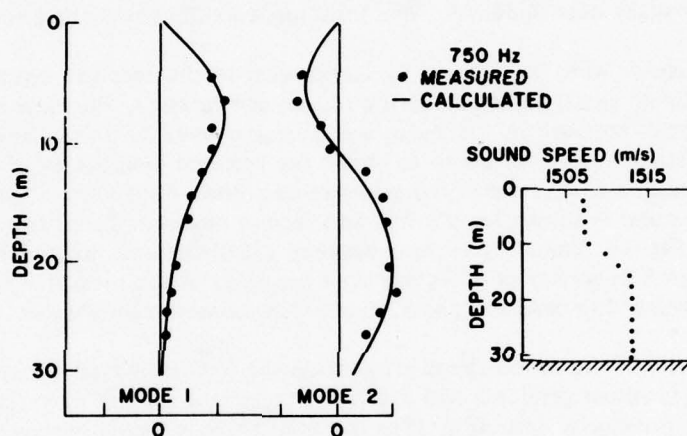
Mode Excitation

From Eq. (65) we note that if range and receiver depth are held constant, the dependence of the pressure amplitude of the nth mode on the source depth is
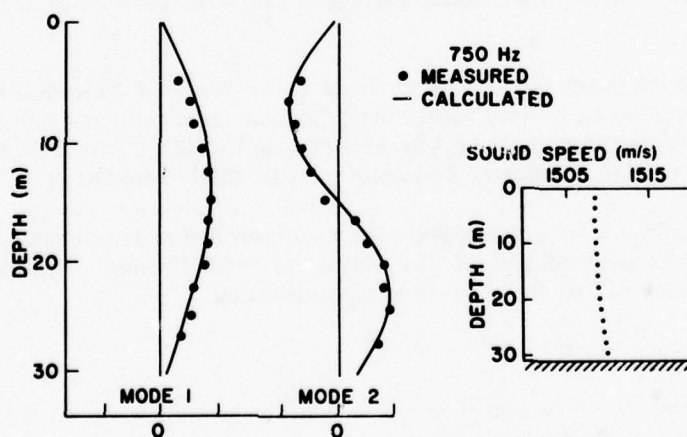
$$P_n(\zeta_0) \propto u_n(\zeta_0), \tag{73}$$

33
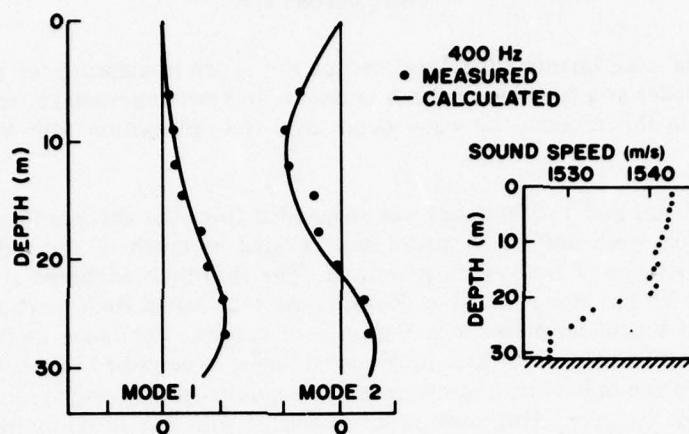
(a) At 400 Hz with a downward refracting profile

(b) At 750 Hz with an upward refracting profile

(c) At 750 Hz with a nearly isovelocity profile

Fig. 19 — Comparison of measured and calculated amplitude functions
(arbitrary scales) for the first and second modes

34

where $\zeta_0 = z_0/H$. That is, the degree to which a given mode is insonified is proportional to the eigenfunction at the source depth. In verifying this proportionality, we encounter two problems which were not present in the measurement of the pressure-amplitude distribution.

The first problem is that measurements involving a number of source depths are not simultaneous. A set of runs at source depths throughout the water column may require a measurement interval of an hour or more, in which time the velocity structure of the water column, and hence the eigenfunctions, may change.

The second difficulty arises from the necessity of inferring the excitation of a mode at the source location from measurements made at some distance away, frequently several nautical miles. If irregularities in the duct boundaries or changes of velocity profile with range results in exchange of a significant amount of energy among the normal modes of propagation, the excitation of a mode at the source cannot be obtained directly from the pressure observed at the receiver.

The experimental arrangement was similar to that described in the preceding subsection. Individual modes of propagation were resolved using the dispersion of short signal pulses along a constant-depth propagation path. Mode orders in the received field were identified by looking for signal phase changes in depth on oscillographic recordings. A single receiver was then selected for each mode, and the variation in signal strength of that mode with source depth was determined. Results [20,21] at the Panama City, Florida, site for the first three modes at 750 Hz are shown in Fig. 20. The absolute value of the eigenfunction is plotted, since the phase changes associated with the axis crossings were not observable. The results verify the proportionality in Eq. (73). The plotted observed signal strength does not vanish at the predicted nulls. The vertical motion of the ship (± 1 m) prevented holding the source at the node of the eigenfunction, so this departure from the predicted result is not considered a serious discrepancy.

Fig. 20 — Measured and calculated dependence of mode excitation on source depth for the first three modes at 750 Hz with the sound-speed profile shown
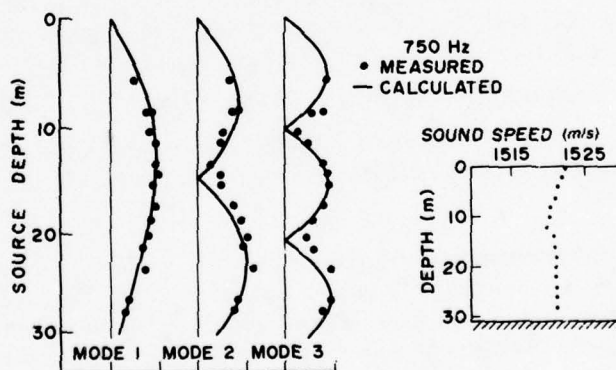
Results similar to those shown were obtained for the few lowest order modes at 400 Hz and at 1500 Hz. Agreement of predicted and calculated signal-strength variation with source depth was also obtained at the Campeche Bank site [13].

Measured signal strengths of individual modal fields usually show variations from pulse to pulse. The standard deviations of the signal strength are typically 3% to 10% of the mean value

and may be attributed to the motion of the source and of the receivers caused by surface waves or to signal contamination by background noise. On some occasions long-term (several-minute) variations of as much as 10 dB have been observed. These variations could not be attributed to noise contamination or transducer motion.

During the July 1969 and March 1970 experiments near the Panama City site such anomalous long-term variations were observed in the modal signal strengths at individual hydrophones and in the responses of spatial filters matched to the first and second modes. The signals were found to vary smoothly by as much as 8 dB over an interval of 7 minutes. To determine whether these variations were characterized by changes in the vertical pressure distribution or by changes in the total energy appearing in the modal field, coefficients of correlation between the signal received by a single hydrophone and the response of the spatial filter were calculated [23]. Correlation coefficients of 0.72 to 0.92 were obtained for the first mode. The second-mode data yielded correlation coefficients of 0.56 and 0.92.

These results indicate that the observed variations were primarily variation in total energy carried in the mode rather than changes in the vertical pressure distribution associated with the mode at the receiver. Apparently the variations are caused by changes in the modal excitation and/or modal attenuation due to changes in oceanographic conditions along the propagation path.

Mode Attenuation

Method

The shallow-water environment is inherently an attenuating medium; an acoustic signal will always suffer loss as it propagates. Furthermore, according to normal-mode theory (as discussed in an earlier section), each modal field will be attenuated differently and can be characterized by a mode attenuation coefficient δ_n which is the imaginary part of the eigenvalue k_n. Thus Eq. (13), expressed as the pressure of a single modal field $20 \log |P_n(r,z)|$ in decibels, modified for attenuation, and after introduction of the free field source level S, becomes

$$20 \log |P_n(r,z)| = S + 20 \log [(2\pi)^{1/2} \rho_1 k_n^{-1/2} u_n(z_0) u_n(z)] - 10 \log r - \alpha_n r. \quad (74)$$

The second term on the right-hand side expresses the effect of source and receiver depth, the third term is cylindrical spreading, and the last term is the mode attenuation term with

$$\alpha_n = (20 \log e) \delta_n,$$

the mode attenuation coefficient in decibels per unit length. Thus, if the pressure of a single mode is measured at a known source depth z_0, receiver depth z, and range r for a known source level S, and if the eigenfunction $u_n(z)$ and eigenvalue k_n are calculated from theory (provided the sound speed and the density in the water and bottom are sufficiently well known), then α_n can be calculated from Eq. (74).

Equation (74) is valid for a point source radiating at a constant frequency, but in our experiments short pulses were used to separate the modes. Since the shallow-water duct is a dispersive system, the length of the pulse increases and the maximum pressure amplitude decreases as the pulse propagates. This effective attenuation of the pulse is accounted for by adding the expression $10 \log [T_0 (T_0 + \Delta T_n)^{-1}]$ to Eq. (74), where T_0 is the pulse length at

36

the source and ΔT_n is the change in pulse length at range r. To derive this expression, it has been assumed, as for a square pulse, that the square of the pressure amplitude of a normal-mode component of the propagated pulse is inversely proportional to the pulse length. The change in pulse length ΔT_n can be calculated from the bandwidth of the source and the computed group velocities.

In some cases, when the modes could not be completely separated, the spatial-filtering technique was used. An equation similar to Eq. (74) can be derived, using the output of the mode filters instead of the pressure at a single hydrophone, from which α_n can be calculated [15].

Results

Measurements of mode attenuation were made off Panama City and on Campeche Bank. In each area, the water depth was nearly constant over the propagation tracks, and the bottom was smooth. The bottom in the Panama City area was hard-packed sand, and the Campeche Bank bottom was semiconsolidated limestone covered by irregular thin patches of fine sand. This difference is significant, as will be seen later.

The earlier measurements at Panama City were made under variable conditions, and it was necessary to use all the terms in Eq. (74) to calculate α_n. Errors are introduced by the approximations of the theory as well as uncertainties in the measured quantities such as the source level S. For the later measurements at Panama City and all the measurements on Campeche Bank a technique was used which eliminated some of these errors. The measurements were made at a number of range stations at the same source and receiver depth and over a time short enough that the environmental conditions remained nearly constant. Thus the measured pressure levels, corrected for cylindrical spreading and dispersion (the latter correction is usually small), plotted as a function of range should fall on a straight line whose slope gives the mode attenuation coefficient α_n. An example is shown in Fig. 21, measured at the Panama City location. The figure shows corrected pressure levels for the first two modes at 400 Hz. The slopes of the lines give $\alpha_1 = 0.61$ dB/km and $\alpha_2 = 1.58$ dB/km. Assuming the bottom can be represented by a single fluid layer, the plane-wave attenuation coefficient of the

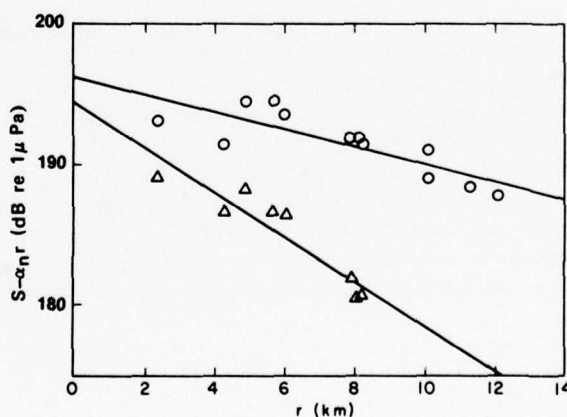Fig. 21 — Typical plot used in determining the mode attenuation coefficient α_n. This example is a plot of Panama City data for the first two modes at 400 Hz, with circles indicating the first mode and triangles indicating the second mode.

37

bottom $\epsilon = \epsilon_2 = \epsilon_3$ can be calculated from Eqs. (22), (23) and (24) . From the first mode we obtain $\epsilon = 135$ dB/km, and from the second mode we obtain $\epsilon = 121$ dB/km, results which are consistent and within the range of measured values.[24]

According to Eq. (22)

$$\alpha_n = \epsilon \gamma_n,$$ (75)

where $\gamma_n = \gamma_n^{(1)} + \gamma_n^{(2)}$. If we assume that

$$\epsilon = \epsilon_0 f^m,$$

where ϵ_0 is independent of the frequency f, it follows from analysis of all the Panama City data that $m = 1.75$. This can be seen from Fig. 22, which is a plot of α_n vs $f^{1.75}\gamma_n$ for all modes and frequencies (400 and 750 Hz). Fitting the points to a straight line gives $\epsilon_0 = 2.8 \times 10^{-3}$ dB/km. Thus we have that

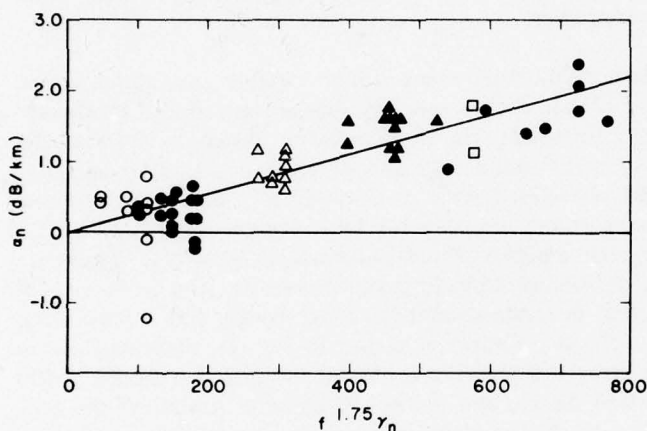$$\epsilon = (2.8 \times 10^{-3}) f^{1.75} \text{ dB/km.}$$ (76)

Fig. 22 — Mode attenuation coefficients α_n determined (as shown in Fig. 21) from the Panama City data for all observed modes at 400 Hz (solid symbols) and 750 Hz (open symbols). Circles indicate the first mode, triangles indicate the second mode, and squares indicate the third mode. The straight line is a least-squares fit, which gives the bottom attenuation coefficient ϵ as expressed in Eqs. (76) and (75).

The frequency dependence of the bottom attenuation coefficient ϵ expressed in Eq. (76) falls within the range of values determined by other methods [25-27]. However Hamilton [24] concludes that the attenuation coefficient of natural marine sediments should vary linearly with frequency. A possible cause of the discrepancy may be the value of c_2, the sound speed of the bottom, used in the analysis. The value used, $c_2 = 1589$ m/s was obtained from bottom-reflection measurements[28] made earlier. According to the literature the type of sediment composing the bottom in the Panama City area should have a sound speed of about 1700 m/s. The bottom attenuation coefficient ϵ is calculated from the measured mode attenuation coefficient by use of Eq. (75) which involves γ_n. The quantity γ_n is calculated theoretically and strongly depends on c_2; thus an error in the assumed value of c_2 could cause significant error in ϵ.

38

Attenuation measurements were made at two stations on Campeche Bank over two tracks at each station. The measurement technique was the same as the later Panama City measurements, with results obtained using signal frequencies of 400, 750, and 1500 Hz.

The measured mode attenuation coefficients however could not be reconciled with a theoretical treatment based on a fluid bottom, as they could for the Panama City data. The bottom consisted of consolidated or semiconsolidated limestone covered with irregular thin patches of sand. The compressional-wave sound speed of the bottom was determined from ground-wave measurements to be 1900 m/s, in agreement with previously reported measurements [29].

Such a compressional-wave speed leads one to expect a higher shear-wave speed than is characteristic of unconsolidated sediments, yet probably lower than the minimum sound speed in the water column, so that the generation of shear waves in the bottom could be an important attenuation mechanism. Unfortunately the NRL normal-mode program was designed to handle only cases in which the shear-wave speed is greater than the minimum sound speed in the water column, when there is total reflection at the bottom for some angles and discrete normal modes exist. It was possible however, by considering the finite shear-wave speed of the bottom to be a small perturbation on the fluid case, to derive an approximate expression for the mode attenuation coefficient [13]:

$$\delta_n = \rho_1 \frac{u_n^2(H)x_n}{8k_n} \left[1 + \left\{ \frac{\rho_1}{\rho_2} \frac{y_n}{x_n} \right\}^2 \right] [1 - |R_n(k_n)|^2], \tag{77}$$

where

$$x_n = [\omega^2/c_1^2(H) - k_n^2]^{1/2},$$
$$y_n = [k_n^2 - \omega^2/c_2^2]^{1/2},$$

and $R_n(k_n)$ is the plane-wave reflection coefficient at the water/bottom interface. All the quantities in Eq. (77) are calculated from the unperturbed two-fluid model except $R_n(k_n)$, which is calculated from the usual expression (as given in Ref. 30 for example) for the plane-wave reflection coefficient at a fluid/solid boundary. It was found that a shear-wave speed of 1000 m/s gave fairly good agreement with the data. The measured and calculated mode attenuation coefficients are given in Table 1.

It can be seen from the table that propagation at station B differs from station A in two respects. First, the attenuation of the lower modes at station B is generally higher than at station A; second, whereas at all three frequencies the first mode at station A has the least attenuation, at station B a higher mode is least attenuated. Both these effects are predicted by the theory. A detailed discussion of the Campeche Bank results can be found in Ref. 13, and the Panama City data are discussed in Ref. 15.

Range-Dependent Environments

In the model discussed, the restriction that the acoustical properties of the medium be range-independent permitted the separation of the acoustic wave equation into two ordinary differential equations, one containing only the depth coordinate and the other containing only

Table 1 — Measured and calculated mode attenuation
coefficients at the Campeche Bank site (Fig. 15)

Frequency (Hz)	Track Direction	Mode Attenuation Coefficient δ_n (dB/m)					
		Mode 1		Mode 2		Mode 3	
		Meas.	Calc.	Meas.	Calc.	Meas.	Calc.
Station A							
400	East	3.7	3.4	—	8.8	—	—
	West	—	3.7	—	—	—	—
750	East	2.1	1.9	—	5.0	—	—
	West	2.0	2.0	—	5.3	—	—
1500	East	1.2	1.1	2.0	2.1	—	3.9
	West	1.6	1.1	—	2.6	—	—
Station B							
400	East	—	7.8	—	—	—	—
	West	—	5.8	—	—	—	—
750	East	—	7.0	1.8	2.1	—	6.6
	West	—	5.3	4.5	3.9	—	4.9
1500	East	—	3.4	—	8.3	—	1.6
	West	—	2.7	—	5.9	—	6.0

the radial coordinate. These equations were solved separately, and the solutions were combined to obtain the description of the acoustic field. If the environment is range dependent, the wave equation cannot be separated rigorously, making the solution of the wave equation considerably more difficult. Since exact solutions for the range-dependent problem do not exist, approximation techniques are necessary.

If the environment changes sufficiently slowly with range, we may obtain approximate solutions based on the constant-depth normal-mode model. To do this, we make two assumptions. The first assumption is that the mode index is conserved over the propagation path [16,17]. If this assumption is correct, energy propagating in any normal mode is not transferred to another mode by the range-dependent environment. The second assumption is that at any point along the propagation path the local properties of the individual normal modes, such as vertical pressure distribution, may be obtained from the constant-depth model, using the environment at the point of interest. Thus the normal mode is assumed to adapt to the local environment.

If this approximation is valid, we may obtain quantities such as the local vertical pressure distribution, the local wavenumber k_n, and the local attenuation coefficient directly from the range-independent model. Description of the acoustic field over an extended region may require the independent solution of Eq. (72) at many points.

To calculate transmission loss over some track in a range-dependent environment, we need in addition to the quantities discussed a method of determining the amount of energy carried in each of the allowed normal modes. In the range-independent model the excitation

of each mode is proportional to the value of the modal eigenfunction at the source depth. The modal excitation in the range-dependent model is calculated similarly, using the eigenfunctions calculated from the environment in the vicinity of the source. This approximation, which is difficult to verify directly by experiment, is similar to the approximation used in obtaining the local pressure distribution. The obstacle to experimental verification is that the modal excitation is inferred from measurements not near the source but at sufficient distance from the source for dispersion to effect modal separation of the signal pulse. To interpret the results of such an experiment, we must assume that the nonuniformity of the propagation path did not convert energy from one mode of propagation to another.

In November 1973 an experiment, similar to the one described in connection with Fig. 19 for a constant-depth path was carried out over two sloping-bottom tracks [22]. Measurements were made of the dependence of the pressure amplitude of individual modal fields on source depth and on receiver depth. The source stations were chosen to have a local acoustic environment different from that at the receiver. Results for the first-order mode at 400 Hz are shown in Fig. 23. On the downslope propagation path (Fig. 23a) the receiver was at zero range and source stations were at ranges 9 and 17 km. The water column exhibited an essentially isovelocity sound-speed profile over the track. At zero range the measured dependence of the pressure amplitude on receiver depth for source depth 18 m at range 9 km (dots) is compared with the eigenfunction calculated from the constant-depth model and the receiver's local environment. Similar agreement was obtained for the modal pressure distribution at zero range when the source was operated at other depths at this 9-km-range station and at the 17-km-range station.

The dependence of the pressure amplitude of the first-order mode on source depth, keeping receiver depth and range fixed, is plotted (squares) at the source range in comparison with the eigenfunction calculated from the constant-depth model and the environment at that range. At both range stations variation in signal strength with source depth agreed with calculated eigenfunction, indicating that over this track the assumption of adaptation of the mode to the local environment and the neglect of mode coupling were justified. Similar agreement was obtained for the second-order mode. No higher-order mode was identified in the signal propagated over this track.

The experiment was repeated using another bearing. On this bearing water depth increased with range and the sound-speed profile changed from a slight negative gradient near the receiver to a strong negative gradient at the source stations, the gradient becoming stronger with increasing range.

Data from the three source stations occupied are shown in Fig. 23b. At zero range a typical observed pressure dependence of the first mode on receiver depth, keeping the source depth and range fixed, is compared with the eigenfunction calculated from the constant-depth model and the receiver's environment. The vertical distribution of pressure is seen to have adapted well to the receiver environment in spite of the considerable change in the shape of the eigenfunction along the track (solid lines at nonzero range).

Comparisons of the dependence of the pressure amplitude on source depth, keeping receiver depth fixed, with the eigenfunction calculated using the source station's environment is shown in the plots at nonzero range. Good agreement is found at the 8-km-range station and for the deeper source positions at the 12-km station.

41
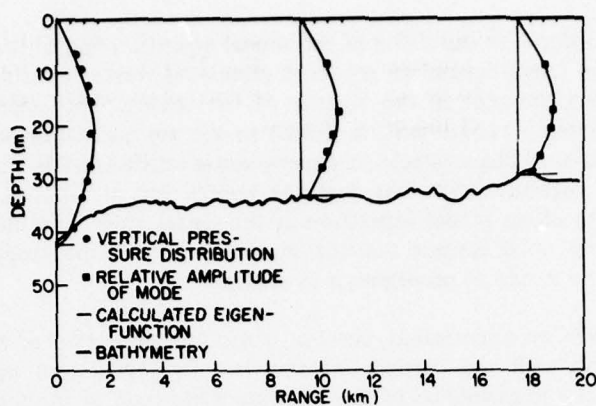
(a) Track with gradually changing depth
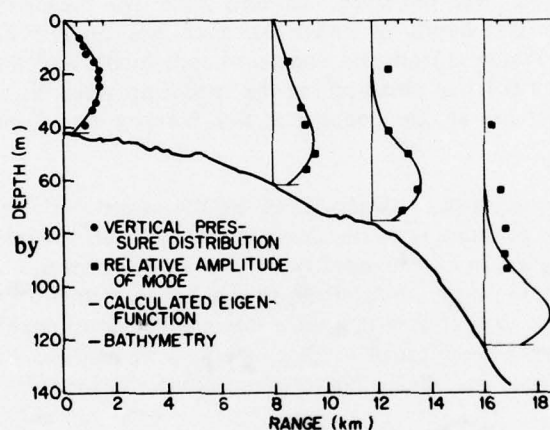
(b) Track with rapidly changing depth

Fig. 23 — Mode amplitude functions for the first mode at 400
Hz over tracks with changing depths

Similar measurements were made for the second-order and third-order modes on this track. In all cases the vertical pressure distributions at the receiver agree well with the eigenfunctions calculated using the receiver's environment. The dependence of signal strength on source depth did not agree in all cases with that predicted by the constant-depth model using the environment at the source. Agreement was best for the first-order mode at the 8-km and 12-km stations. Agreement was poor for the first-order mode at the 16-km station and for the second-order and third-order modes at all stations. Lack of agreement between the predicted and calculated source-depth dependence of the modal pressure indicates either that the approximation of local separability is not valid or that the modes of propagation are coupled with

changing environment. The bottom slope is no greater at the 8-km and 12-km stations than at the receiver on the downslope propagation track (Fig. 23a), for which track the approximation of local separability was found to be valid. The presence of mode conversion therefore appears to be the more probable cause of the disagreement.

The results of this experiment indicate that realistic models of transmission loss in continental-shelf waters with range-dependent environments may have to include the effects of mode conversion.

A comparison of measured transmission loss (dots) and loss calculated using the range-dependent model is shown in Figs. 24a and 24b. In the experiment two CW projectors, one operated at 29 Hz and the other at 121 Hz, were towed radially from the receiver (at zero range) along a track which traversed a bank. Bathymetry along this track is shown in the lower illustrations. The calculated loss was obtained from the incoherent mode sum. The coherent mode sum showed interference effects of the same magnitude (10 to 15 dB) as the scatter in the data; thus the scatter can be attributed to modal interference phenomena.

Calculated loss is seen to be in fair agreement with the measurements. Loss increases slowly to range 95 km. Beyond that range loss increases rapidly. The 5-dB discontinuity in the 29-Hz loss associated with the decrease in source depth at range 61 km is also seen in the calculated loss. Some details of the measured loss differ from results of calculations. Loss measured at 29 Hz is $\simeq 5$ dB less than that calculated at range 58 km, and the discontinuity in the loss in Fig. 24b predicted at range 61 km is not reflected in the measurements. These discrepancies are not considered serious, since information regarding bottom composition was available only at the endpoints of the track. Errors in the assumed ocean-bottom structure rather than errors in the model may account for the discrepancies at intermediate points.

Thus, in spite of the indications of mode conversion derived from observations of individual normal modes, the transmission-loss model employing the adiabatic approximation produced results in fair agreement with experiments.

Numerical Results from the Scattering Model

Reflection Coefficients

In the theory section we derived an expression for the reflection coefficient of a rough ocean surface which is described by an rms height and a wave-height power spectrum which describes the spatial characteristics of the ocean surface. We also derived an expression for the reflection coefficient in the Kirchhoff limit (discussion following Eqs. (45) and (46)). We note here that in the Kirchhoff limit the mean value of the reflected field does not depend on the directional properties of the ocean surface [12] but depends on just its rms height.

We now present some calculated results for reflection from an ocean surface described by the Pierson-Moskowitz wave-height spectrum[31]. This model describes a fully developed sea and does not include long-range swell components which might have sufficient regularity to simulate a deterministic diffraction grating. The ocean-surface frequency spectrum we use is given by

$$\Phi(\Omega,\phi) = (2/\pi)\Phi(\Omega)\cos^2\phi, \ 0 \leqslant |\phi| < \pi/2$$
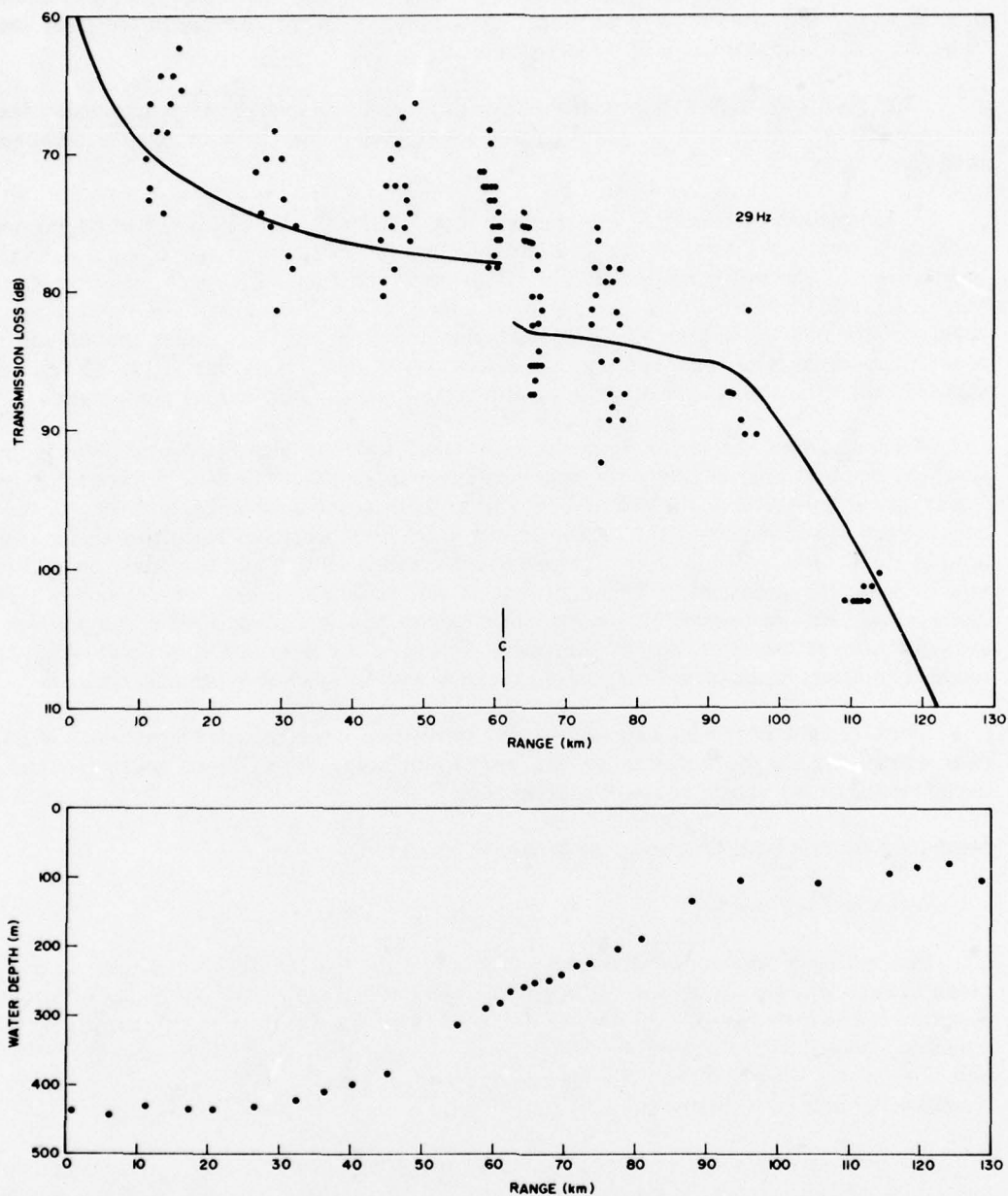$$= 0, \ \pi/2 \leqslant |\phi| \leqslant \pi,$$

43

Fig. 24a — Acoustic transmission loss at 29 Hz (top) and bathymetry (bottom) over a sloping-bottom track. The dots are measurements, and the curve is the calculated loss. At 61 km range (marked C) both sources were raised to accommodate changing bathymetry
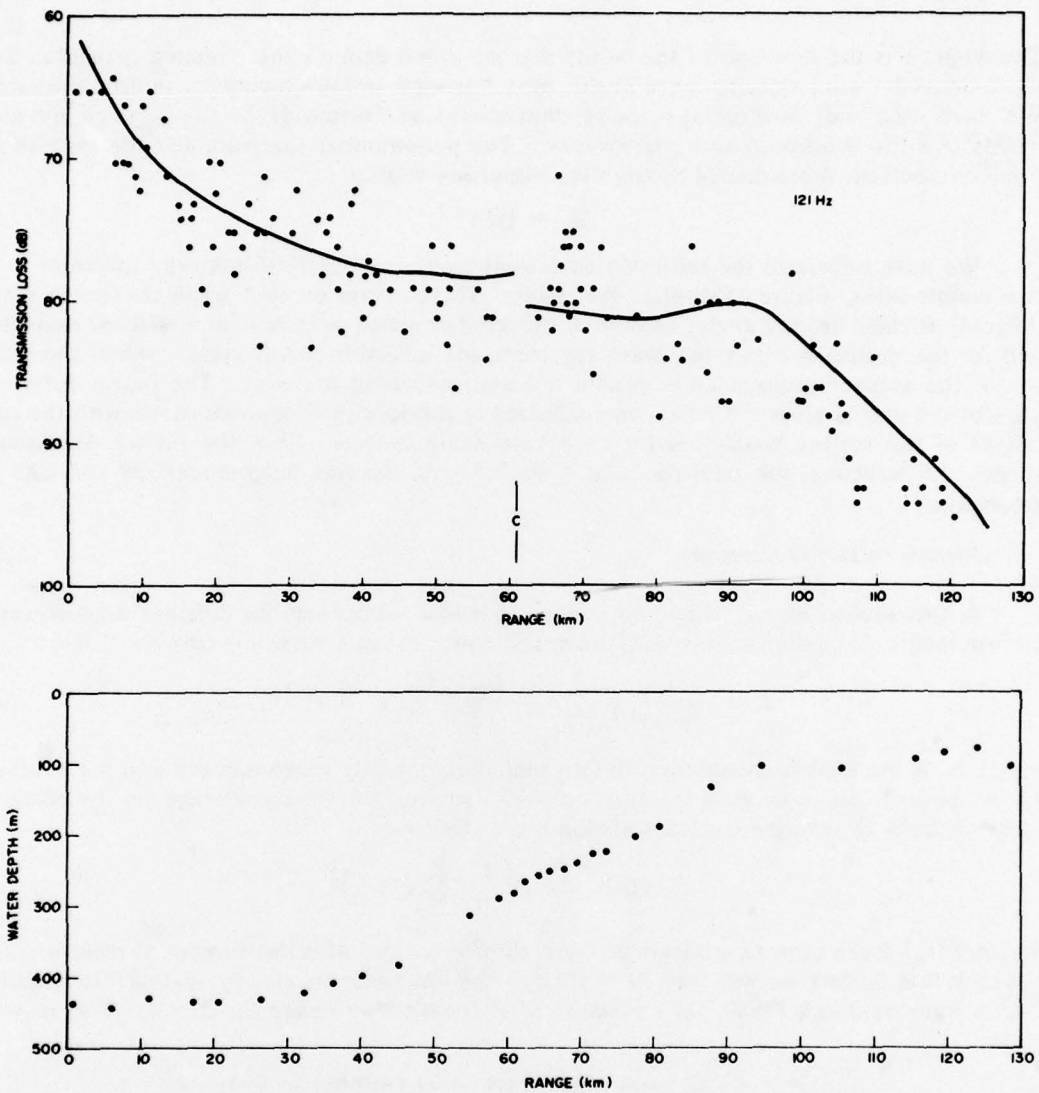
44

Fig. 24b — Acoustic transmission loss at 121 Hz (top) and bathymetry (bottom) over a sloping-bottom track

where

$$\Phi(\Omega) = 0.0081 \, g^2 \Omega^{-5} e^{-0.74 \, (\Omega_0/\Omega)^4}$$

The angle ϕ is the direction of the wind; that is, $\phi = 0$ denotes the direction parallel or antiparallel to the wind velocity, since in this model upwind and downwind are indistinguishable. We have used the same cosine-squared dependence as Fortuin [32]. Ω_0 is given by g/U, where U is the windspeed and g is 9.8 m/s^2. The wavenumber spectrum and the frequency-number spectrum Φ are related through the dispersion relation

$$\Omega = (g\xi)^{1/2}.$$

We have calculated the reflection coefficient using the Pierson-Moskowitz spectrum for a few sample cases. Figure 25 displays the results. Three curves on each graph are for the three different acoustic bearing angles relative to the wind direction as indicated. For these examples and for this particular directional wave spectrum, the reflection loss is greatest when the bearing of the acoustic propagation is parallel (or antiparallel) to the wind. The fourth curve on each of the graphs gives the reflection coefficient in the Kirchhoff approximation, with the rms height of the surface roughness for each case being obtained from the Pierson-Moskowitz model. In particular, for windspeeds of 5 and 15 m/s, the rms heights are 0.09 and 0.85 m respectively.

Attenuation Due to Scattering

In this section we present some transmission-loss calculations for different shallow-water environments. Including attenuation, the acoustic pressure at a range r is (see Eq. (13))

$$P \simeq \frac{\omega \rho_1}{(8\pi r)^{1/2}} \sum_{n=1}^{N} \frac{u_n(z_0) u_n(z)}{k_n^{1/2}} e^{ik_n r} e^{-\delta_n r},$$

where δ_n is the total attenuation coefficient including not only roughness but also the effect of a lossy bottom. Since we are concerned only with attenuation, we can average out the effect of receiver depth by defining our transmission loss as follows:

$$TL \equiv 10 \log \left[\frac{1}{M} \sum_{m=1}^{M} P^2(z_m) \right],$$

where $P(z_m)$ is the acoustic pressure at the mth receiver and M is the number of receivers; for the case that follows we will take $M = 10$ with the ten receivers equally spaced throughout a 100-m water column. Finally, as a measure of attenuation we define the function Γ at range r to be

$$\Gamma_{s,b} = r^{-1} [TL(\text{with roughness}) - TL(\text{without roughness})],$$

where the subscript s or b refers to surface or bottom roughness, since we will deal with each one separately. The units of Γ are dB/km; Γ is a measure of attenuation of the total acoustic field due to scattering with geometric spreading and bottom loss eliminated. It is unfortunately a range-dependent quantity, but at a given range it is indicative of the importance of the total scattering loss whereas the scattering coefficients of the individual normal modes do not indicate the strength of the excitation of the normal modes. We now present some numerical calculations of Γ for different shallow-water environments. Most of the results are for surface scattering loss, but we also present some results for bottom scattering.

46

(a) Windspeed = 15/ms; frequency = 750 Hz
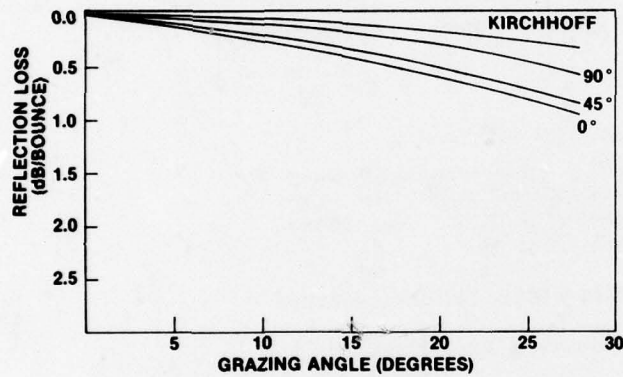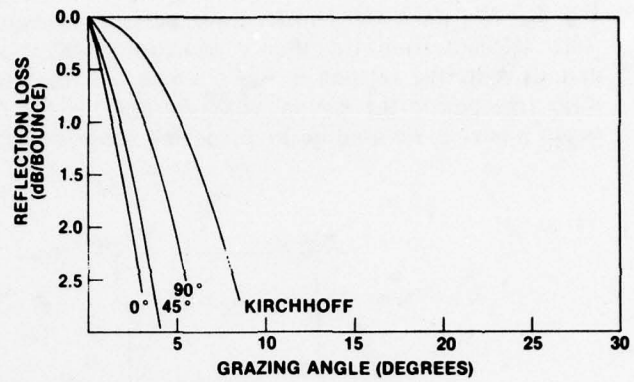
(b) Windspeed = 5 m/s; frequency = 750 Hz
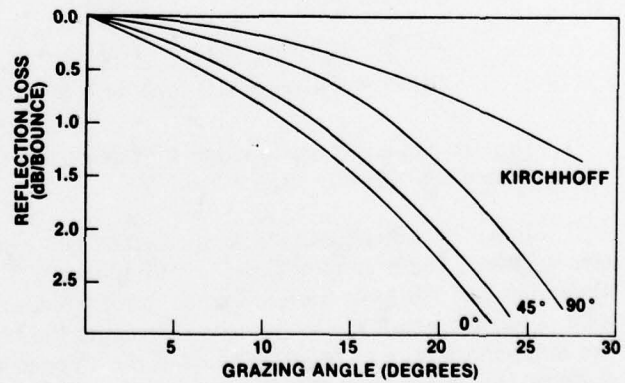
(c) Windspeed = 5 m/s; frequency = 1500 Hz

Fig. 25 — Reflection loss from an ocean surface described by the Pierson-Moskowitz model of a fully developed sea. The angles 0°, 45°, and 90° are acoustic bearing angles relative to the direction of the wind. The Kirchhoff result for a surface with the same rms height is also shown.

47

These calculations can be performed for an arbitrary range-independent sound-speed profile. For the work presented here we have chosen the three generic profiles as shown in Fig. 26. We have also chosen three bottom-sediment types as listed in Table 2. These types were selected from Hamilton's acoustic classification of marine sediments [24]. Hamilton defines K by the relation $\alpha = Kf$, where α is the attenuation coefficient in dB/m for a plane wave traveling in the bottom sediment and f is the frequency in kilohertz. We use the same ocean model as we used in the preceding subsection for the reflection coefficients.
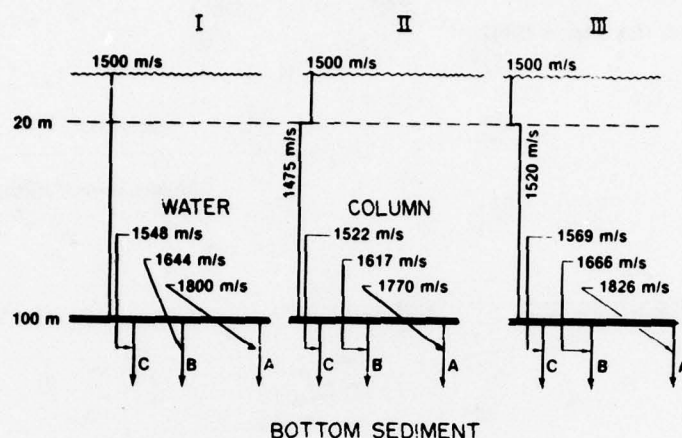

Fig. 26 — Isovelocity (I), downward refracting (II), and upward refracting (III) sound-speed profiles used in the transmission-loss calculations. A, B, and C are sediment types as listed in Table 2.

Table 2 — Properties of three bottom sediments

Sediment	Sound-Speed Ratio c_2/c_1	Density (ρ_2) (g/cm^3)	K*
A. Coarse sand	1.201	2.03	0.46
B. Silty sand	1.096	1.83	0.65
C. Sand-silt-clay	1.032	1.58	0.20

*Hamilton [24] defines K by α(dB/m) = K f(kHz).

We have evaluated the function Γ_s using the Pierson-Moskowitz spectra for a few sample cases. These are shown in Figs. 27 and 28.

Figure 27 shows some results at 50 Hz. The results for profile II (Fig. 27a) are for negative profiles. These cases indicate a saturation effect after a certain wind velocity is reached. Cases IIA and IIB have four and three normal modes respectively, of which only one in each case is trapped below the thermocline. Because the other modes that interact with the surface are stripped away, we are left with only the trapped mode, which does not interact with the surface. Hence we have this saturation effect. Case IIC has only one mode, which is barely trapped below the thermocline; therefore no surface loss should be observed. Figure 27b illustrates the results for an upward refracting profile. There is no saturation effect. Case C is
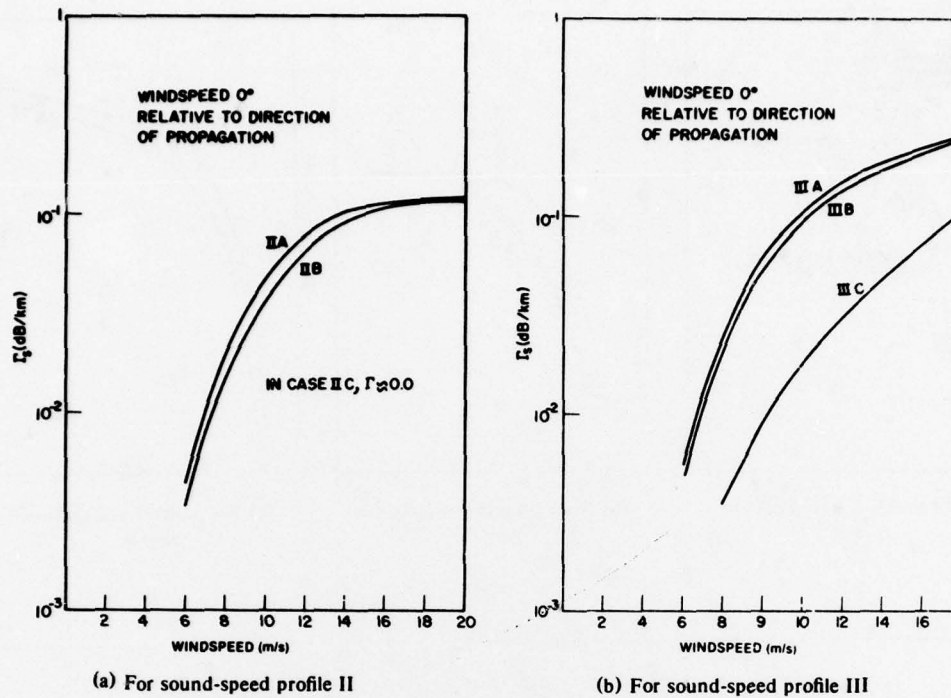
48

(a) For sound-speed profile II

(b) For sound-speed profile III

Fig. 27 — The function Γ_s at 50 Hz and range $r = 25$ km versus the windspeed for sediment types A, B, and C

significantly different from cases A and B, indicating the importance of bottom type when calculating surface loss.

Figures 28 shows sample results at 500 Hz. This figure includes the effect of wind direction relative to the bearing of acoustic propagation. The calculated results indicate a large surface loss along the direction of the wind.

Figures 28a and 28b are for negative profiles and again indicate the saturation effect. However saturation occurs at a significantly lower windspeed than for the same cases at 50 Hz. Even more significant is case IIC (Figs. 27a and 28b); at 50 Hz there is no interaction with the surface and hence no surface loss, but at 500 Hz there is surface interaction and hence surface loss. No saturation effects are predicted in Fig. 28c and 28d, which are for isovelocity profiles, or in Figs. 28e and 28f, which are for an upward refracting profile. For these profiles, particularly the upward refracting profile, the surface loss is significant when compared to the bottom attenuation due to the lossy bottom sediments. The transmission loss with bottom attenuation for these profiles was about 70 dB, of which 5 to 10 dB can be attributed to the lossy bottom sediments. For the isovelocity profile for windspeeds greater than about 10 m/s the surface contribution to transmission loss begins to exceed 5 dB at this 25-km range. For the upward refracting profile the surface loss is much larger.
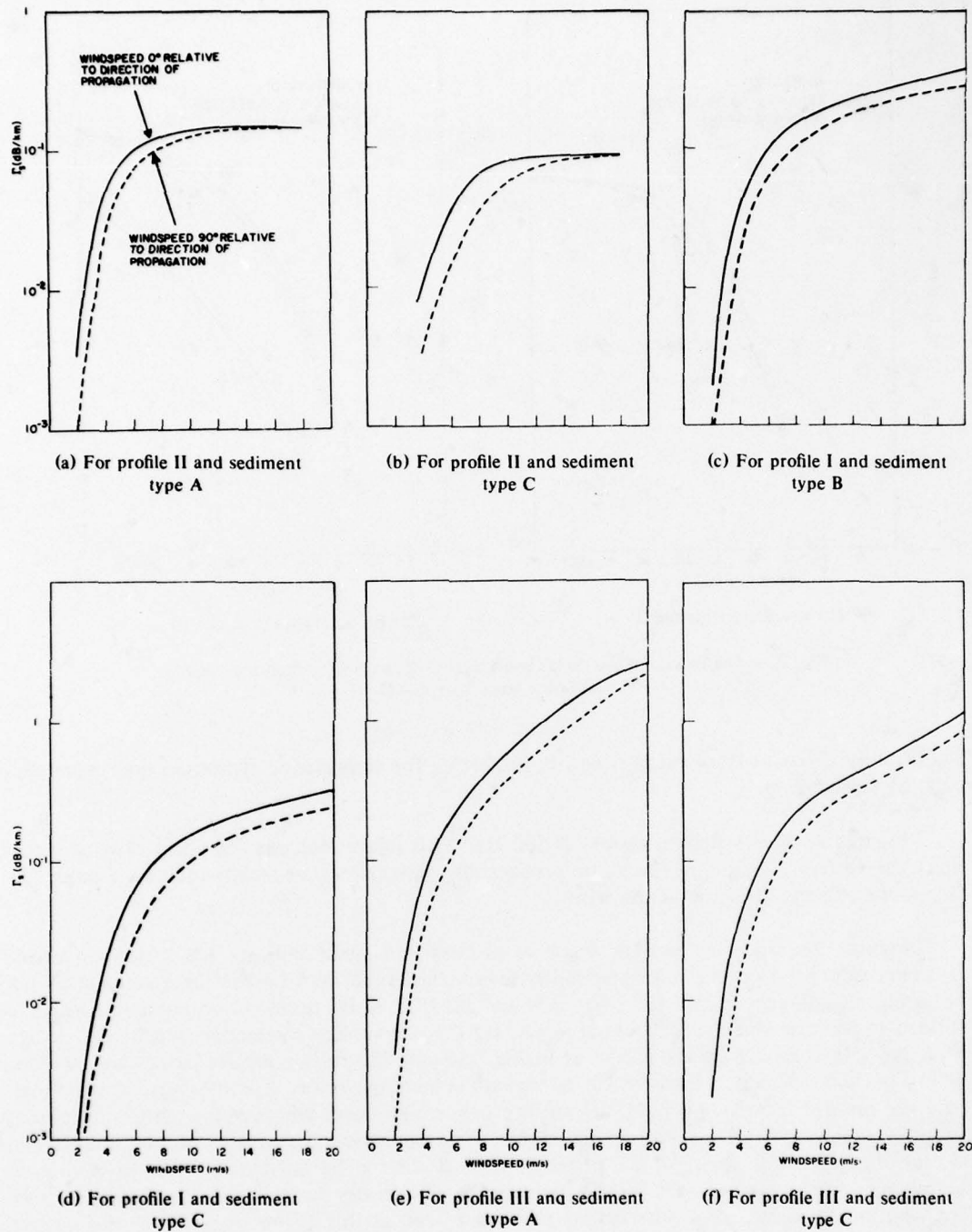
49

(a) For profile II and sediment
type A

(b) For profile II and sediment
type C

(c) For profile I and sediment
type B

(d) For profile I and sediment
type C

(e) For profile III and sediment
type A

(f) For profile III and sediment
type C

Fig. 28 — The function Γ_s at 500 Hz and $r = 25$ km
versus the windspeed

50

Figure 29 is an example of some results for the case when the ocean bottom is rough and the ocean surface is smooth. In this figure both curves are calculations made using the bottom parameters associated with coarse sand. The calculations were was made in the Kirchhoff limit. The curves indicate a greater loss for the negative profile than for the positive profile. There is no saturation effect, because for this case no mode was trapped in the upper layer, so that all modes interacted with the bottom. When the acoustic wavelength is such that the water column supports a surface duct, the saturation effect will appear.
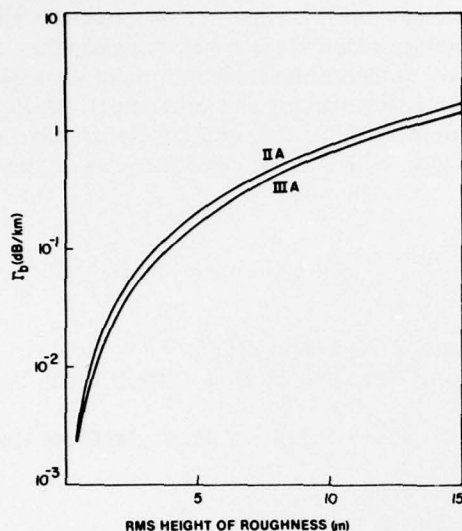
Fig. 29 — The function Γ_b at 50 Hz and $r = 25$ km versus the rms height of the bottom roughness for profiles II and III and sediment type A

CONCLUSIONS

Any mathematical model of a real physical phenomenon, to be tractable, must employ approximations for the physical properties of the environment. The suitability of those approximations depends on the precision with which the phenomenon needs to be predicted. In the case of acoustic propagation in shallow ocean water the principal environmental conditions of concern are the conformation, structure, and acoustic properties of the seabed and of the overlying water. Determining the needed complexity in modeling these features has been approached by an iterative process involving trial models and at-sea measurements. The wave equation for the physical model is solved by numerical methods and implemented on a high-speed general-purpose computer. The computer program is formulated to predict for each modal field the level of excitation, the pressure amplitude distribution with depth, and the attenuation with range. The total acoustic field is then obtained for any field point by summing the modal fields at the appropriate range and depth. The models have been evaluated in at-sea experiments in which special techniques were used to resolve individual modal fields, which were then examined to determine the excitation, amplitude distribution, and attenuation as functions of frequency, source depth, and range. Measurement results were compared with predictions to determine the adequacy of the model and to provide guidance for further refinement if necessary.

51

It has been demonstrated that the model in its present state of development can in most cases predict the signal field with sufficient detail and accuracy to be a useful tool for system design, performance prediction, and tactics. Certain recognized problem areas remain. The most serious of these are in predicting the field in an environment (sound-speed profile in the water, water depth, and bottom properties) which changes rapidly with range and in obtaining estimates of bottom properties to be used as inputs to the model.

The techniques developed for examination of individual modal fields and the data obtained in the experimental program described in this report together with the resulting models provide a technology base for further exploratory development in shallow-water acoustics. The basic propagation model constitutes the core of technology required for systems applications. It is an intrinsic part of ambient-noise and reverberation models and serves as a point of departure for developing a knowledge for higher order effects (fluctuations and coherence), which is essential for performance prediction. The areas of noise, fluctuations, and coherence have as yet received little attention in shallow-water studies. There is a strong need for work in these areas.

REFERENCES

1. I. Tolstoy and C.S. Clay, *Ocean Acoustics,* McGraw-Hill, New York, 1966.
2. C.L. Pekeris, "Theory of Propagation of Explosive Sound in Shallow Water," Geol. Soc. Am. Mem. **27** (1948).
3. W.M. Ewing, W.S. Jardetzky, and F. Press, *Elastic Waves in Layered Media,* McGraw-Hill, New York, 1957.
4. W.A. Kuperman, J. Acoust. Soc. Am. **58**, 365-370 (1975).
5. W.A. Kuperman and F. Ingenito, J. Acoust. Soc. Am. **61**, 1178-1187 (1977).
6. F.G. Bass, Izv. Vyssh. Uchebn. Zaved Radiofiz. **4**, 476-483 (1961) (JPRS: 10223).
7. W.C. Meecham, J. Rational Mech. Anal. **5**, 323-333 (1956).
8. C. Eckart, J. Acoust. Soc. Am. **25**, 566-570 (1953).
9. P. Beckmann and A. Spizzichino, *The Scattering of Electromagnetic Waves from Rough Surfaces,* Pergamon, New York, 1963.
10. C.S. Clay, J. Geophys. Res. **71**, 2037-2046 (1966).
11. H. Medwin and J.D. Hagy, Jr., J. Acoust. Soc. Am. **51**, 1083-1090 (1972).
12. L. Fortuin, J. Acoust. Soc. Am. **52**, 302-315 (1972).
13. F. Ingenito and S.N. Wolf, J. Acoust. Soc. Am. **60**, 611-617 (1976).
14. C.S. Clay, J. Acoust. Soc. Am. **36**, 833-837 (1964).
15. F. Ingenito, J. Acoust. Soc. Am **53**, 858-863 (1973).
16. A.D. Pierce, J. Acoust. Soc. Am **37**, 19-27 (1965).
17. D.M. Milder, J. Acoust. Soc. Am **46**, 1259-1263 (1969).
18. A.O. Williams, Jr., and M.N. Lewis, Research Analysis Group (Brown University) Tech. Report 56-1, May 1956.
19. J.F. Miller and F. Ingenito, "Normal Mode FORTRAN Programs for Calculating Sound Propagation in the Ocean," NRL Memorandum Report 3071, June 1975.
20. R.H. Ferris, F. Ingenito, and A.L. Faber, "Experimental Separation and Identification of Acoustic Normal Modes in Shallow Water," NRL Report 7174, Oct. 30, 1970.
21. R. H. Ferris, J. Acoust. Soc. Am. **52**, 981-988 (1972).
22. S. Wolf, Saclantcen Conference Proceedings No. 17, Part 7, pp. 34-1 to 34-9, 1975.
23. A. F. Schuetz, "Some Measurements of Acoustic Normal Mode Propagation in Shallow Water," NRL Report 7493, Nov. 16, 1972.

24. E.L. Hamilton, Geophys. **37**, 620-646 (1972).
25. L.D. Hampton, J. Acoust. Soc. Am. **42**, 882-890 (1967).
26. B.F. Cole, J. Acoust. Soc. Am. **38**, 291-297 (1965).
27. G. Shumway, Geophysics **25**, 451-467 (1960); Geophysics **25**, 659-682 (1960).
28. R.H. Ferris and W.A. Kuperman, "An Experiment on Acoustic Reflection From the Sea Surface," NRL Report 7075, May 28, 1970.
29. J. Antoine and J. Ewing, J. Geophys. Res. **68**, 1975-1996 (1963).
30. L.M. Brekovskikh, *Waves in Layered Media,* Academic Press, New York, 1960, p. 31.
31. W.J. Pierson, Jr., and L. Moskowitz, J. Geophys. Res. **69**, 5181-5190 (1964).
32. L. Fortuin, "The Sea Surface as a Random Filter for Underwater Sound Waves," Ph.D. dissertation, Uitgevrij Waltman, Delft, the Netherlands, 1973.